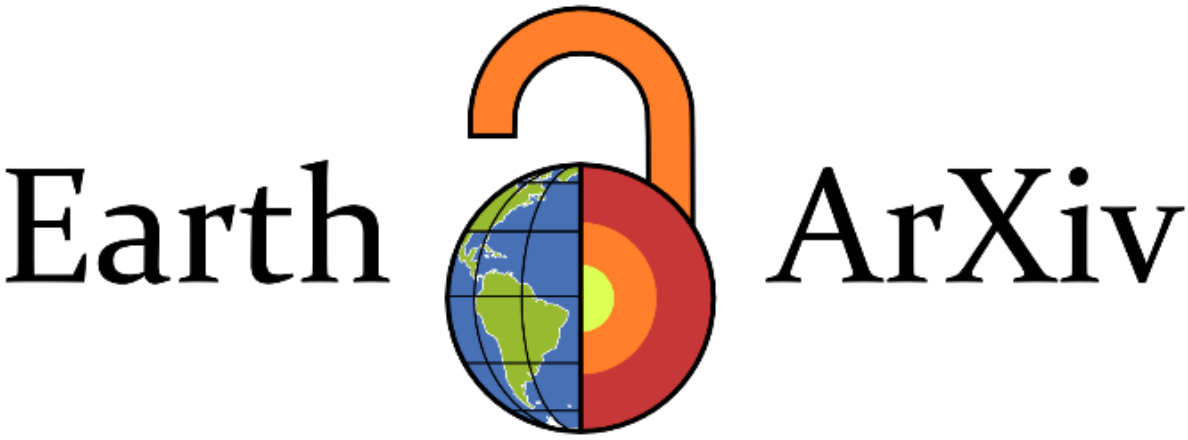

Shifting Patterns of Summer Humid Heatwaves Highlight Growing Threat over South Asia and Middle East–North Africa

Saptashree Deb[1], *Sparsha Rajesh Sherke*[1], *Poulomi Ganguli*[1]

[1]Indian Institute of Technology Kharagpur, Kharagpur, India
Email: debsaptashree@kgpian.iitkgp.ac.in

Peer review status:

This is a non-peer-reviewed preprint submitted to EarthArXiv. This manuscript is currently under review at Climate Dynamics (Manuscript ID: CLDY-D-25-00841) (published by Springer Nature). The version submitted here includes improvements acknowledging the comments provided during the first round of review (First round of revision submitted on 21.01.2026).

Shifting Patterns of Summer Humid Heatwaves Highlight Growing Threat over South Asia and Middle East–North Africa

Saptashree Deb[1], Sparsha Rajesh Sherke[1], Poulomi Ganguli[1]

[1]Indian Institute of Technology Kharagpur, Kharagpur, India

Abstract: Humid heatwaves (HHWs), marked by elevated heat−high moisture compounding, are increasingly concerning for sustainable development in South-Asia (SAS) and the Middle East–North Africa (MENA). We examine the spatiotemporal compounding of HHWs during summer (March−August) across 268 urban and peri-urban sites within the IPCC–reference regions in the SAS and MENA using in-situ observations. We investigate roles of two heat–humidity indices—wet-bulb temperature (T_x^w) and extended heat-index (H_x) to analyze changes in the distribution properties of HHW attributes over two distinct timeframes: 1980–2000 (TW1) and 2001–2024 (TW2). Over 80% of sites show rising trends in daily median magnitudes for both indices in TW2, while ≤25% exhibit increases in median HHW severity. In contrast, skewness increases across 65% of sites, and inter-arrival time shortens across approximately 60–70% of sites, indicating that median changes alone may not capture increasing frequency and temporal clustering. HHW spatial coverage expands by about 10% per decade during 1980–2024. Post-2000, HHW days across SAS and MENA coincide with stronger mid-tropospheric ridging/blocking, enhanced northwesterly warm-air advection, and elevated atmospheric moisture. Regionally, SAS HHWs are characterized by reduced outgoing longwave radiation, increased cloud cover, enhanced sensible heat flux, and weak latent heat flux anomalies. In contrast, MENA shows a markedly different regime, dominated by clear-sky, subsidence-driven desert environments, together with moisture-influenced coastal zones. MENA coastal regions show weaker sensible heat flux but stronger latent heat flux, which can enhance urban-coastal humid heat and inland thermal stress through advection.

1 Introduction

The 21st century has recorded the warmest years ever (NASA Earth Observatory 2019; Perkins-Kirkpatrick and Lewis 2020; Saha et al. 2025). In recent decades, humid heatwaves (HHWs) have emerged as one of the deadliest natural hazards, severely impacting human health, agriculture, and energy systems (Russo et al. 2017; Raymond et al. 2020; Wang et al. 2022; Gramling 2022). HHW is a period of extreme heat with high humidity, making it difficult for the body to cool down, leading to heat stress and potential health hazards (Buzan & Huber 2020; Matthews 2018; Raymond et al. 2020; Baldwin et al. 2023; Kjellstrom et al. 2009). Elevated heat stress in crops could be amplified due to delays in harvesting owing to human perceived heat stress, underscoring the need for comprehensive monitoring and early warning systems (Simpson et al. 2021). Recent reports from the World Meteorological Organization (WMO 2025) highlighted that Asia is experiencing more intense and persistent record-breaking heatwaves in recent decades. The South Asia (SAS) and Middle East and North Africa (MENA) regions are one of the deadliest hotspots of heatwaves (Pal and Eltahir 2016; Im et al. 2017; Zittis et al. 2021; Tandon 2024). Between 1992 and 2020, heat-related mortality in the SAS exceeded 25,000 (WMO 2022), whereas the MENA has witnessed a notable rise in heatwave frequency and intensity since the mid-1990s (Godard 2008; Russo et al. 2016;

Perkins-Kirkpatrick and Lewis 2020; Meque et al. 2022). Further, recent assessments (Javed 2023; de Bont et al. 2024) on projected changes in heatwaves have suggested that the SAS could experience over 30 record-breaking HHWs in the coming decades, whereas the annual heat-related mortality rate in the MENA tends to reach up to about 124 per a hundred thousand people (Hajat et al. 2023). As humid heatwaves increasingly threaten human health and the environment, understanding their spatiotemporal characteristics and driving mechanisms in the South Asian Subcontinent (SAS) and the Middle East and North Africa (MENA) is essential.

So far, several studies have investigated heatwave mechanisms locally, *e.g.*, in India (Rohini et al. 2016; Kumar & Mishra 2019; Rashid et al. 2023; Ghatak et al. 2017; Van Oldenborgh et al. 2022; Devi et al. 2023; Zachariah et al. 2021), in MENA (Fontaine et al. 2013; Varela et al. 2020; Hajat et al. 2023) and at a global scale (Röthlisberger and Papritz 2023; Jiang and Xu 2025). However, most of these studies have focused solely on dry-bulb temperatures for assessing heatwaves, neglecting the role of humidity in amplifying heat stress. Several assessments (Matthews 2018; Rashid et al. 2023; Meque et al. 2022; Russo et al. 2016; Raymond et al. 2021) have examined physical processes and trends related to dry heatwaves on a regional scale. Despite some progress, only a limited number of studies have systematically analyzed changes in humid heatwave characteristics and the associated large-scale climatic patterns that drive these shifts over time in the South Asian (SAS) and Middle Eastern and North African (MENA) regions, highlighting a significant knowledge gap.

The Intergovernmental Panel on Climate Change Sixth Assessment Report (IPCC AR6 2021) has reported low to medium confidence in hot extremes in North and West Africa, whereas higher confidence was reported for those in the Mediterranean and the SAS. Using re-analysis and climate model simulations, Wang et al. (2021) demonstrated that, globally, the mean wet-bulb temperature (T_w) is higher in the tropics and mid-latitudes (excluding the high-latitude Tibetan Plateau) compared to the high-latitude areas during the historical period (1981 − 2005). Furthermore, in the warming scenarios (RCP4.5 and 8.5), a greater relative increase in mean values and variability is projected (from 2076 to 2100) over the tropics, while a higher absolute increase in mean is projected over the mid-latitudes. Likewise, a few previous assessments (Speizer et al. 2022; Birch et al. 2022; Engdaw et al. 2022; IPCC 2023; Ngoungue Langue et al. 2023) have primarily relied on reanalysis-based proxy observations instead of in-situ observations to analyze heatwaves. The review of the literature (Raymond et al. 2020; Wang et al. 2021; Freychet et al. 2020; Zhang et al. 2024) suggests that HHWs are highly localized in space and time, which reanalysis datasets tend to underestimate, especially across the tropics and sub-tropics. Gridded observations and global to regional climate models (up to 2.5^{o}) also fall short in capturing regional dynamics and synoptic patterns of HHWs (Di Cecco & Gouhier 2018; Engdaw et al. 2022; Hajat et al. 2023; Hamed et al. 2024; Rashid et al. 2023). These gridded observations tend to underestimate extremes due to the artefacts of spatial interpolations, especially in data-sparse regions and mountainous terrains (Rogers et al. 2021; van Oldenborgh et al. 2022). Further, climate model outputs often inadequately capture specific

humidity trends, especially in arid and semi-arid regions, due to over/underestimation of its key variables, atmospheric water vapor and sea level pressure (Christensen et al. 1997; Raäisaänen 2007; Zhao et al. 2015; Simpson et al. 2024).

Based on the observational analysis, so far, a large body of the literature has investigated global and regional changes in temperature extremes since the 1950s (Brown et al. 2008; Zhang et al. 2011; Zhou and Ren 2011; Stephenson et al. 2014; Kim et al. 2016; Xie et al. 2019; Saleem et al. 2021). Although regional-scale heatwaves have been widely analysed (Wang et al. 2018; Shafiei Shiva et al. 2019; Feron et al. 2019; Vogel et al. 2020), but these studies are biased to specific regions, particularly focusing on Europe, North America, South America, and Australia. In other regions of the globe, the characterisation of heatwaves and their associated atmospheric patterns has been limited by sparse and good quality of observational records, complex topography and/or the performance of reanalysis products (Frich et al. 2002; Luo et al. 2019). A few assessments have shown asymmetric changes toward extreme temperature distributions in projected time windows (Kodra and Ganguly 2014; Xie et al. 2019). However, discrepancies among climate models in capturing land-atmospheric feedback further complicate the magnitude of temperature and their shifts over the global tropics (Freychet et al. 2021). SAS and MENA have been underrepresented in most of the global-scale assessments, leading to fewer region-specific early warning systems. Although few studies have proposed heat warning systems for HHWs in Europe and Australia (Lowe et al. 2011; Nairn et al. 2022), efforts to develop a heatwave warning system in the SAS and MENA are primarily based on air temperature, with little emphasis on heat−humidity compounding.

Furthermore, most of the assessments (Donat and Alexander 2012; Whan et al. 2014; Di Cecco and Gouhier 2018; Gedefaw 2023) have analyzed either changes in mean or extremes. Further, several studies have used a single metric, either humidity integrated with a temperature-based indicator, *e.g.*, T_w (Raymond et al. 2017; Bekris et al. 2023) or heat index (Rothfusz 1990) metric to assess the heat stress linked with HHWs. The T_w is the lowest temperature achievable through the saturation of water into an air parcel at a constant pressure (Bekris et al. 2023). However, in several regions of the SAS and MENA, the "uncompensable heat stress"— in which the body is unable to achieve sufficient heat dissipation through sensible, latent, and radiative pathways to maintain a stable temperature, is shown to occur at a much lower value than the threshold limit of $T_w \sim 35$°C (Ivanovich et al. 2022; Justine et al. 2023). The heat index formulation proposed by Rothfusz (1990) was used in an operational forecast in several regions globally (Xu et al. 2021; Marcotullio et al. 2021; Ha et al. 2022; Dajuma et al. 2024). However, this heat index computation is based on polynomial approximation of temperature and relative humidity together, which is reported to underestimate the heat stress magnitude by the order of 10ºC when extreme temperature and humidity jointly co-occurred, which is more common in the SAS and MENA (Lu and Romps 2023). So far, very few assessments have systematically investigated HHWs and their characteristics from an extreme event perspective, focusing mainly on changes in daily mean

air temperature and its variability, such as in Schär and Chiriatti (2025). Changes in higher order statistical moments of HHWs can affect its upper tail behaviour affecting the severity and frequency of the record HHW events. Unlike other assessments, which primarily relied either on a single heat–humidity quantity (*e.g.*, T_w in Bekris et al. 2023 and Raymond et al. 2020) or only analyzing daily air-temperature extremes (*e.g.*, Ye and Fetzer 2019 and Schär and Chiriatti 2025) across temperate climate regions, this study offers the first observational assessments of in-depth statistical characterization of HHWs using two well-defined heat–humidity indicators. While a few studies (Dubey et al. 2021a; Lekshmi et al. 2026) have investigated large-scale drivers of dry heatwaves over the SAS in general and the Indian subcontinent in particular, and climate model projections over the MENA (Lelieveld et al. 2016; Malik et al. 2024) region, a comprehensive assessment involving multiple climate variables across climate sub-regions in the two deadliest global heatwave hotspots, i.e., SAS and MENA, remains largely unexplored in the heatwave literature. Hence, we attempted to link these changes to large-scale atmospheric circulation patterns, considering multiple climatic variables that drive HHW conditions, leading to pronounced spatiotemporal compounding of heatwaves in recent times.

To bridge the knowledge gaps, using in-situ observational records, we have systematically assessed the shifts in HHW attributes over the selected IPCC reference regions (Iturbide et al. 2020) in the SAS and MENA by comparing two non-overlapping time windows: recent (2001-2024; hereafter, TW2) versus the retrospective (1980-2000; hereafter, TW1). The selected time windows align with the existing assessment by Dong et al. (2024). We consider 268 urban and peri-urban sites (Figure 1a) based on the literature, their heatwave severity, and quality of in situ available records (see details in Table S1). The objective of this paper is two-fold: (1) To identify distributional shifts in the first and higher-order statistical moments of heatwave attributes considering two different revised HHW metrics, such as modified Wet Bulb Temperature and an extended Heat Stress Index, which account for the integrated effect of high temperatures and elevated humidity; (2) To understand the role of key physical mechanisms in shaping the spatiotemporal compounding (Zscheischler et al. 2020) nature of HHWs. We evaluate heatwave events that co-occur in neighboring locations, which can lead to spatially compounded HHWs. Additionally, we examine the trend in sequential occurrence of HHWs in close succession, leading to their cumulative impact, rather than the isolated and discrete occurrences over a longer interval. Our analysis framework is presented in Figure 1b. The derived insights will aid in an improved understanding of shifts in HHWs and related attributes in recent time windows, enabling precise and timely heatwave hazard preparedness, and supporting climate adaptation practices in the changing climate.

2 Materials and Methods

2.1 Study Area

The analysis focuses on SAS and the broader MENA domain, with regional definitions guided by the IPCC AR6 WGI reference regions (Iturbide et al. 2020). SAS spans approximately ~5°–30° N and ~60°–95° E, encompassing the Indian subcontinent and adjoining monsoon-

influenced areas. Out of the 268 cities examined in this analysis, 39 are located in SAS. MENA, on the other hand, comprises a few key IPCC subregions that represent the dominant subtropical arid–semiarid climates and adjacent transition zones, including the Mediterranean (MED), Sahara (SAH), Arabian Peninsula (ARP), and West Africa (WAF), and extending into West-Central Asia (WCA), together covering approximately ~0°–50° N and ~20° W–80° E. Of the cities considered in our analysis, 229 are situated in the MENA regions.

2.2 Data and Indices

We utilize at-site observational records from the Hadley Centre Integrated Surface Database (HadISD v3.3.1.202306p), which offers quality-controlled station-based sub-daily meteorological records such as dry-bulb and dew point temperatures and sea-level pressures. HadISD database (Dunn et al. 2012) from the UK Met Office offers homogeneous, quality-controlled, in situ sub-daily (ranges from 1- to 3-hourly) observational records of surface meteorological variables, such as near-surface air temperature, dew point temperature, sea level pressure. These dataset implements extensive automated quality control checks to discard sites with excessive typographical or instrumental errors or individual occurrences of such issues. The datasets have been widely used in several heatwave assessment studies (Smith et al. 2011; Dunn et al. 2016; Hu 2021) at local, regional, and global scales. We further procured at-site hydrometric observations across the SAS region, particularly in India, from the IMD's Data Supply Portal, (https://dsp.imdpune.gov.in/data_supply_service.php#procedure) at a sub-daily timescale of 3-hourly intervals, sampled between 8:30 a.m. and 5:30 p.m. Indian standard time (3:00 to 12:00 hr UTC). These sites were selected based on data completeness and availability of meteorological records. Subsequently, we discarded several sites that failed to pass the robust quality-control procedures following an earlier literature (Raymond et al. 2020). To analyze and contrast the physical mechanisms that influence HHWs in two distinct time windows, we obtain large-scale atmospheric variables, such as geopotential height, wind components, and specific humidity, all at a 500 hPa from the ERA5 archive, available at a 0.25° spatial resolution. The choice of geopotential height at 500 hPa is based on the fact that the review of the literature (Pfahl and Wernli, 2012; Brunner et al., 2017; Jiménez-Esteve and Domeisen, 2022, Uckan et al. 2024) suggests that this pressure level is, overall, the most relevant driver of hot extremes, which is often linked to the emergence of atmospheric blocking, impacting the large-scale circulation in the mid-troposphere, and thereby contributes to HHW development.

2.3 Humid Heatwave Metrics and Identification of Heatwave Events

We calculated two heat−humidity metrics from the at-site daily maximum values that account for both temperature and humidity together: (1) the human-perceived extended heat stress Index (humidex), H_x (Lu & Romps 2023), which incorporates a thermoregulatory model, and (2) the Wet-Bulb Temperature (T_x^w) obtained using the Revised Davies-Jones algorithm (Rogers and Warren 2024; Raymond 2023). We consider the maximum of the sub-daily values to capture peak heat stress for each day, referring to this as the "daily" time series throughout.

We validated the derived T_x^w against IMD-observed daily maxima WBT for the summer months (Mar–Aug, consistent with our HHW season) at four representative stations across the Indian subcontinent, namely, Hissar (located in Northern India, 29.179°N, 75.755°S), Surat (located in Western India, 21.2°N, 72.833°S), Kolkata (located in Eastern India, 22.655°N, 88.447°S), and Thiruvananthapuram (located in South India, 8.483°N, 76.95°S). We assessed the agreement between observed and calculated T_x^w using the non-parametric rank-based Spearman's rank correlation (ρ) (Ye et al. 2015) and Root mean square error (RMSE). The comparison shows a very strong correlation, ranging from $\rho \approx 0.998–0.999$, with negligible errors (RMSE ≈ 0.16–0.35 °C) across all sites (Fig. S1), indicating the credibility of calculated T_x^w in capturing observed wet-bulb temperature anomaly. We have considered the Boreal summer season, spanning from March to August, when the temperature reaches its peak across the SAS and MENA (Varela et al. 2022; Aadhar and Mishra 2023; Saha et al. 2023; Malik et al. 2024b; Jackson et al. 2025; Neethu and Abish 2025).

We define an extreme HHW event (See Fig. 1b for details) — ET_x^w and EH_x derived from T_x^w and H_x, respectively, when the daily maximum values of the at-site heat stress metrics, T_x^w and H_x, exceed the daily variable threshold of the 90th percentile and remain persistently above this threshold consecutively for more than three days or longer (Perkins and Alexander 2013; Perkins-Kirkpatrick and Gibson 2017). For variable threshold determination, 366 (an additional day considering leap day of the year) T_x^w- and H_x-duration curves were developed using continuous daily maxima T_x^w and H_x series. Next, a centered mean moving window of 31 days (± 15-day) was employed as a smoothing filter to eliminate short-duration events (Russo et al. 2014). We assess the severity of each event using the daily accumulated humid heatwave magnitude index (HWMId) for both ET_x^w and EH_x (Lo et al. 2021; Russo et al. 2014; see SI S1.1 for details).

2.4 Evaluation of Shifts in Humid Heatwave Attributes

We compare shifts in the median, a measure of central tendency and higher-order statistical moments (e.g., variance, autocorrelation, and skewness) for daily maxima heat–humidity series and corresponding HHW event characteristics, such as severity, frequency and areal coverage of heatwaves, across the two non-overlapping time windows (1980-2000 versus 2001-2024). The choice of the two non-overlapping time windows (TW2: 2001–2024 versus TW1: 1980–2000) with a break point around the year 2000 because the post-2000s, the decade between 2000 and 2009, is reported to be the warmest years in the instrumental record (UN 2010; KNMI 2010). Second, several sites across the MENA region either lack observations or contain records with substantial data gaps before the 1980s. The similar time windows have been adopted in previous studies (*e.g.,* Saha et al. 2025; Dong et al., 2024) to examine heatwave extremes over the Northern Hemisphere. Consequently, our assessment complements and extends the existing analyses of HHW extremes. Changes in skewness indicates an asymmetrical shift in the distribution of humid-heat event magnitudes beyond changes in mean condition (Kodra and Ganguly 2014; Ye and Fetzer 2019). For instance, an increase (or

decrease) in skewness is typically associated with a transition toward a heavier (or lighter)-tailed distribution, implying a higher (or lower) likelihood of rare, high-magnitude extreme humid heatwaves and a lower (or higher) likelihood of more modest or near-normal events. We then evaluate the statistical significance at a 10% significance level throughout to relax the power of the statistical evaluation, which aligns with earlier literature (New et al. 2006). Next, we evaluate the shifts in distributions of heatwave metrics between the two time windows using the Jensen-Shannon (JS) divergence, shown from 0° to 50°N, capturing the influence of the boreal summer (Menéndez et al. 1997; Dhinakaran 2023) measure (See SI S1.2 and Table S2 for details). We evaluate the trends in annual frequency and spatial extents of HHWs using the least-square linear regression fit, and statistical significance was evaluated using the F-test at a 10% significance level.

We examine the temporal compounding nature of HHW events derived from H_x and T_x^w series using the following measures: (1) Lag-1 autocorrelation of daily series. Changes in autocorrelation describe how the dependence pattern of a time series on its past values evolves, quantifying the temporal clustering of daily heat-humidity extremes. An increase (decrease) in lag-1 autocorrelation indicates stronger (weaker) short-term persistence or memory, implying that rare HHWs tend to cluster (or move apart) within a short time window, leading to shorter (longer) recovery times between events (Baldwin et al. 2019). Further, an increase in autocorrelation in HWMId may also be linked to an increase in localized warming conditions (Martinez-Villalobos et al. 2025). Next, (2) trends in the time between two consecutive HHW events, *i.e.*, the inter-arrival time between two sequential occurrences that measures the duration between the termination of the first heatwave event and the beginning of the next event (see Figure 1b). In our analysis, the number of non-HHW days, describing the inter-arrival time between two successive HHW events ranges from $N_I \in [2, n)$, where N_I is the inter-arrival days, with 2-day being the least, while, n is the highest possible number of days, with $n \leq 180$ considering the summer period (March to August). We then determined at-site trend in inter-arrival time using the non-parametric Sen's slope estimator (Agarwal et al. 2021; Deb et al. 2025; SI S1.3), and evaluated trend significance via bootstrap resampling with N=5000 iterations. The trends in at-site autocorrelation and inter-arrival time will aid in evaluating whether events are clustered more closely or tend to become sporadic over time.

2.5 Understanding Physical Mechanisms of Humid Heatwaves

To investigate the physical drivers underpinning the observed shifts in HHW attributes, we compare the composite anomaly of large-scale climate features, *e.g.*, geopotential height, specific humidity, wind patterns, outgoing longwave radiation (OLR), total cloud cover (TCC), latent heat (LH) and sensible heat (SH), during the heatwave and non- heatwave days, considering each metric across the nonoverlapping time windows. All anomalies were calculated relative to a 30-year climatological baseline (1991–2020) (WMO 2017), consistent with recent climate attribution studies.

3 Results

3.1 Distinct Trends in Daily versus Humid Heatwave Events

Figure 2 compares the shifts in the median and variability of heat−humidity quantity between TW2 and TW1 for the indices, T_x^w and H_x series. Most of the cities across the complete domain, show a significant at-site increase in daily median in ~80% of sites (206 out of 268; Figure 2a) for T_x^w and ~92% (246 out of 268; Figure 2b) of sites for H_x, respectively. SAS shows an increase in daily at-site median in ~82% of sites (32 out of 39; Figure 2a) for T_x^w and ~92% (36 out of 39; Figure 2b) of sites for H_x, respectively, suggesting an intensification of daily heat−humidity magnitude along with relatively broader and flatter distributions (panel (b) of Figures S2 and S3). Likewise, MENA shows an increase in daily at-site median across ~76% of sites (174 out of 229; Figure 2a) for T_x^w and ~91% (210 out of 229; Figure 2b) of sites for H_x, an indicate an overall increase in at-site median T_x^w (Figure S2a) and H_x (Figure S3a), suggesting an intensification across sub-regions such as the MED**,** WAF, and WCA. We observe relatively broader and flatter distributions (panel (b) of Figures S2 and S3) across the MED and WAF**,** showing an enhanced spatial variability in recent decades. These changes in distribution across two distinct time windows are statistically significant for the MED and WCA, as confirmed by a two-sample Kolmogorov-Smirnov test at the 10% significance level. Furthermore, the changes (TW2 versus TW1) in at-site daily variability in heat−humidity metrics map (Figs. 2c, d) show a significant widespread increase in spatial variability in H_x compared to T_x^w. While shifts in at-site variability show a significant decrease in 71% more cities (Figure 2c) in T_x^w compared to H_x, the spatial distribution of daily variability changes in TW2 for H_x (Figure 2d) shows an increase in 81% more cities than T_x^w. Considering T_x^w, SAS, and MENA exhibit an increase in at-site variability across 15% (6 out of 39) and 22% (50 out of 229) of sites, respectively (Figure 2c, d). In Contrast, considering H_x, SAS and MENA show an increase in at-site variability across 62% (24 out of 39) and 40% (91 out of 229) of sites, respectively (Figure 2c-d). The JS divergence analysis (Figure 2e) shows an elevated heat stress, with prominent peaks observed over the latitudinal bands of 40°N–50°N and from 15°N extending southward up to about 9°N towards the lower latitudes.

In contrast to the daily maxima T_x^w and H_x series, the extreme HHW magnitude, quantified by HWMId (Figure 3) reveals a more localized intensification across regions. SAS shows an increase in median for 5-23% of sites, while MENA shows increase across16-18% of the sites (Figure 3a, b). SAS exhibit an increase in spatial variability up to 20-26% of the sites, while MENA shows 11-18% of the sites (Figure 3c, d), considering ET_x^w and EH_x, respectively. When we observe the complete domain, both ET_x^w (Figures 3a, c) and EH_x (Figures 3b, d) derived HWMId demonstrate an increase in median for 20–21% of sites and an increase in spatial variability at 16–23% of sites. The TW2 marks a substantial increase in the median HWMId considering EH_x. An increase in median HWMId in EH_x often exceeds 1.5°C, with two-fold more sites (> 85 out of 268) experiencing an increase in severity compared to the number of sites experiencing an increase in severity in ET_x^w (42 out of 268) across SAS and

MENA. Further, regional comparison (Figures S4) reveals that approximately 67% (4 out of 6) of the reference climate regions show a larger fraction of sites with an increase in at-site median of HWMId in TW2, for ET_x^w (Figures S4a) and EH_x (Figures S4c), respectively. Increased spatial variability in HWMId during TW2 is observed across 83% (5 out of 6) of the reference climate regions for ET_x^w (Figures S4b) and EH_x (Figures S4d), respectively. This shift remains consistent in both heat−humidity metrics across three major IPCC reference regions (see Figure S4) — the SAS, and the ARP, and WAF subregions of the MENA.

Next, we analyze changes in skewness (Figure 4) for HWMIds for both ET_x^w and EH_x across SAS and MENA. Figure 4 shows the spatial distribution of differences in HWMId for the recent versus retrospective periods for both ET_x^w (Figure 4a) and EH_x (Figure 4b). Approximately 65–66% of sites (177–178 out of 268) exhibit an increase in skewness in TW2 compared to TW1, indicating that hot summers with rare HHW events tend to occur more frequently than expected from the increase in median. SAS shows ~60-74% of sites (23–29 out of 39) exhibit an increase in skewness in TW2 compared to TW1 for both ET_x^w (Figure 4a) and EH_x (Figure 4b). Further, MENA also shows a substantial increase in at-site skewness values ~63-71% of sites (145-162 out of 229) for both ET_x^w (Figure 4a) and EH_x (Figure 4b). To examine the large-scale atmospheric circulation patterns during the top ten hot years with the record HWMId (marked with black-edged circles in Figures 4c, d), we plot the composite anomaly of geopotential height with mean wind vectors for ET_x^w (Figures S5a) and EH_x (Figures S5b). The composite anomalies of geopotential height (Figure S5a) show strong positive anomalies (>5 m), indicating the presence of a persistent upper-level anticyclonic pattern, spanning across SAS and North Africa, ARP, and parts of WCA (Figure S5a). The overlaid mean wind vectors suggest an intensified and stagnant circulation regime over the Tibetan Plateau, SAH, and the ARP regions, favourable for heat entrapment and suppressed convective activity over the MENA and SAS. Geopotential height anomalies of EH_x (Figure S5b) less coherent circulation pattern over the SAS and a relatively weaker and more localized anticyclonic signature over the SAH and MED. In summary, these regional patterns suggest that the severe HHWs are driven by persistent upper-level blocking reinforcing the intensity and persistence of elevated heat−humidity, contributing to the record HHWs in TW2. Similar spatial pattern is found to be prominent for ET_x^w, spatially across inland ARP and central part of the SAS (Figure 4a). A substantial increase in at-site skewness values in HWMId is observed across all six reference climate regions, with at least 45% of cities within each region experiencing increases in skewness based on ET_x^w (Figure S6a) and EH_x (Figure S6b), respectively. Likewise, temporally, we observe a significant upward surge in skewness during post-2000s (Figure 4c) in ET_x^w. The temporal evolution of annual skewness of heatwave severity further shows a significant rising trend in ET_x^w (Figure 4c), at the rate of 1.8/30-year. This is contrasted by a relatively stable changes in EH_x (Figure 4d), reporting a rather declining trend at the rate of −0.3/30-year.

To understand the spatial variability in the number of HHW days across regions, we compared the station-level annual average HHW days for each region using both heat–humidity metrics for the two non-overlapping time windows (2001–2024 vs. 1980–2000). Overall, all regions show the higher annual average frequency of HHW days in the TW2 (Figures S7a, b), with the largest increase evident for the ARP (on average 17–21 days/year), followed by MED in MENA and SAS (on average 15–18 days/year) regions, respectively. Next, to assess whether these record HHW events tend to become more frequent and widespread, we compare an at-site event frequency (Figure 5) of TW2 versus TW1. We observe a robust increasing trend in the relative frequency of HHWs in the TW2 compared to the TW1. Across SAS, considering ET_x^w and EH_x (Figures 5a, b), about ~72% of sites show an increasing trend, whereas 28% of sites show a decreasing trend. However, across MENA, about 80-90 % of the sites show an increasing trend, while only 10-20% of sites exhibit a decreasing trend. Across the entire domain, considering ET_x^w (Figure 5a), about ~78% (22/%) of sites show an increasing (decreasing) trend. For EH_x (Figure 5b), increases in frequency are observed across 91% of sites, while decreases are observed over only 9% of sites. Further, the temporal evolution of HHW event frequency (counts per year) demonstrates a significant rising long-term trend from 1980 to 2024, with ET_x^w showing a stronger increasing trend at a rate of ~13 events/year (Figure 5c) compared to the ~8 events/year in EH_x (Figure 5d). Considering ET_x^w and EH_x, across all climate regions, the MED of MENA shows the largest regional increase of ~5-8 events/year, while the WAF in the same region shows the least increase at the rate of ~0.2-0.3 events/year (Figure 5c).

Figure 6 demonstrates a sharp rise in the area under extreme HHWs from 1980 to 2024, with a significant increase in spatial extent at the rate of 7.6%/decade for ET_x^w (Figure 6a), while 9.7%/decade for EH_x (Figure 6b). The regional trends in spatial coverage of HHWs for the SAS vary in the order of ~1.4% per decade (Figures S8a, b), while ~6–10% per decade for the MENA (Figures S8c, d), for ET_x^w and EH_x, respectively, indicating a more spatially extensive upward trends in humid heatwaves over the MENA in the recent decade.

3.2 Increasing Autocorrelation and Decreasing Trends in Inter-arrival Times of HHWs

To evaluate the temporal compounding behaviour of HHWs, we analyze changes in lag-1 autocorrelation and trends in interarrival time between HHW events.

The changes in lag-1 autocorrelation (TW2 versus TW1) of heat−humidity metrics at a daily temporal scale (Figures 7a, b) show that most sites display an increased autocorrelation in TW2. About 60-73% (160-198 out of 268) of sites show an increase in autocorrelation considering T_x^w (Figure 7a) and H_x (Figure 7b) in the recent time window compared to the retrospective era, suggesting a potential temporal compounding of HHW events. When investigating regionally, an increase in autocorrelation is shown for 60-82% of sites (23-32 out of 39) across SAS and 60-73% of sites (137-166 out of 229) across MENA. As we move from higher latitudes toward the equator (50°N to 0°), the lag-1 autocorrelation shows a notable

increase. Larger autocorrelation increases are spatially clustered between 0° and 10°N latitudes (Figure 7c). About 83% (5 out of 6) of the reference climate regions showed an increased autocorrelation across MENA, with ARP (~75-85%) and WAF (~60-83%) exhibiting the highest changes in T_x^w (Figure S9a) and H_x (Figure S9b).

Further, insights into the temporal compounding can be gained from the trend in inter-arrival time between consecutive HHW events, which reveals a marked decline over the analysis period (1980−2024). The regional variations in median interarrival times (Figure S10) vary from 2 to ~170 days for the SAS and MENA. Among MENA sub-regions, considering T_x^w, the least median inter-arrival time is observed for WAF (13 days), followed by WCA and SAH (17 days) climate reference regions. The spatial distribution of changes in inter-arrival time between HHWs (Figures 7d-e; Figures S11a-b) across the overall domain (SAS and MENA) shows that both ET_x^w and EH_x demonstrate about 60-70% more sites exhibit a significant decreasing trend — a decrease is more prominent for EH_x in which up to 70% (from 15% to 26%; Figure S11) of more sites indicate a significant shortened inter-arrival time in TW2 compared to TW1. Conversely, there is up to 52% (from 19% to 9%) of decrease in the number of sites showing an extended in inter-arrival time (Figure S11b), indicating more sites are experiencing a decrease in inter-arrival time in TW2. When examined regionally, SAS exhibits a significant decreasing trend across ~17-26% of the sites, whereas 10-17% of the sites show a significant increasing trend for both the metrics, ET_x^w and EH_x. Next, MENA demonstrates a significant decrease across 20-29% of the sites, while ~9-11% of sites exhibit a significant increase in trend, for ET_x^w and EH_x, respectively (Figures 7d, e). The latitudinal transect of mean inter-arrival time (days) (0° to 50°N) shows a decrease as we move from 30°N toward the equator (Figure 7f), indicating that at lower latitudes, the transitions between successive HHWs tend. Typically, tropical sites (0° to 23.5°N) show lower mean inter-arrival time ranging from ~2 to 42 days as compared to the sub-tropical sites, which showed the mean inter-arrival times ranging from about 13 to 90 days (23.5°N to 40°N). However, Bangui (4.4°N, 18.5°E), situated in the interior of Central African (CAF), is an exception, showing extended mean inter-arrival times in both metrics, reporting an average of ~45 days in ET_x^w (Figure 7f). Interestingly, this site also reports a lower JS divergence measure in daily heat–humidity series (Figure 2e) compared to sites within 0° to 10°N. Further, we observe most reference climate regions show a significant shortening in inter-arrival times (Figures S12a-b) in both indices. Spatially, the most notable decrease in inter-arrival time is observed over the WAF, followed by SAH in MENA region, reporting up to 50% of sites (Figure S12b) showing a significant reduction in inter-arrival time of HHWs considering EH_x. In contrast, considering ET_x^w, the decrease in inter-arrival time of HHWs is limited to only 30% of the spatial coverage (Figure S12a), with a notable decrease over the SAH, followed by the ARP of MENA region. However, in SAS, the decrease in inter-arrival time is limited to about 20% of spatial coverage across both indices, while increases are confined to only < 10–15% of the sites (Figures S12a-b). While the long-term (1980–2024) trend (Figure 7g, h) in inter-arrival time in HHWs across overall domain (SAS and MENA) is statistically insignificant in both heat metrics, we observe

a robust decline in inter-arrival times during the post-2000s (shown in solid lines in blue). For ET_x^w, the long-term trend shows an insignificant decreasing trend up to ~1.2 days/30-year, while in the post-2000s, it shows a significant declining trend of up to 10 days/30-year (Figure 7g). Likewise, considering EH_x (Figure 7h), the inter-arrival time shows an insignificant long-term decrease of up to ~3 days/30-year, while in the post-2000s, it shows a significant declining trend of up to 9 days/30-year. Furthermore, when examined regionally (Figure S13), considering ET_x^w, we observe that in TW2, the SAS region shows a significant decline in inter-arrival time of up to −21 days/30-year (Figure S13a, b), indicating strong evidence of temporal compounding between two consecutive HHW episodes. In contrast, MENA shows weaker and statistically insignificant decrease in interarrival times up to the order of −7 days/30-year (Figure S13c) considering ET_x^w. Considering EH_x, both SAS and MENA exhibit an insignificant decreasing trend (Figure S13b, d) in inter-arrival times. Despite the long-term trend (1980–2024) in inter-arrival times (Figure S13) being statistically insignificant in both heat-humidity metrics in both regions, a robust decreasing trend emerges for ET_x^w in the SAS during post-2000s, indicating a significant shortening of successive HHW episodes in recent times for this region.

3.3 Compound Shifts in HHW Magnitude and Inter-arrival Time

Shifts in both HHW magnitude and interarrival time reveal growing compound intensification of heat and humidity together in recent time (2000−2024), pointing to vulnerable cities that tend to experience shorter time intervals between successive extreme HHW events, elevating the cumulative and compounding impacts (Zscheischler et al. 2020). The scatter plot relationship (Figure 8) between decadal changes in HHW magnitude and inter-arrival time shows a statistically significant ($p < 0.10$ via F-test) inverse relationship between trends in ET_x^w and EH_x, indicating sites experiencing an increase in HHW magnitude also tend to experience a significant declining in transition times between successive HHWs over the recent decades. Considering ET_x^w (Figure 8a), approximately 24 cities show a significant increasing trend in HHW magnitude accompanied by decreasing inter-arrival time, of which 6 cities are located across SAS and 18 cities across MENA. Among these, ~67% (16 out of 24) of the cities are located within 100 km of the coast, with six cities lying within 10 km, underscoring the elevated heat−humidity compounding experienced by the sites located at low-lying coastal zones. A similar pattern emerges in EH_x (Figure 8b), where 34 cities show a joint trend showing an increase in HWMId (i.e., HHW magnitude) and a decrease in inter-arrival time. Out of these, only one city in SAS shows this joint trend, whereas, the remaining 33 cities are from MENA region. Of these, 63% (22 out of 34) are coastal cities, while 10 are located within ~10 km of the coast. Cities experiencing significant upward trends in HHW magnitude versus shortening of inter-arrival times are predominantly clustered across the MED, SAH, ARP climate sub-regions of MENA, whereas only a limited number of sites across the SAS region. Strikingly, within the MED region alone, four cities, namely, Ustica, Iskenderun, Makedonia and Inebolu show significant trends in upward changes in heatwave severity, along with shortening in inter-

arrival time, even at a 1% significance level and located near to the coast (within 30-km of the coast), suggesting a strong confidence in temporal clustering of HHW events, with elevated HHW magnitude over these coastal sites.

3.4 Physical Drivers of HHW Intensification across the SAS and MENA

Figures 9 and S14 summarize the potential physical drivers associated with the intensification of extreme HHWs across the SAS and MENA, considering ET_x^w and EH_x, respectively.

Over the SAS, Figures 9a, b quantifies the difference in geopotential height anomalies considering ET_x^w between two non-overlapping time windows (TW2–TW1) with (Figure 9a) and without (Figure 9b) HHW days, which is overlaid by statistically significant changes in winds. An anomalously high geopotential height during TW2 potentially contributes to the development of blocking highs (persistent high-pressure zones), which elevates extreme HHWs. These blocking systems, together with strengthened winds can weaken the monsoonal circulation especially over the Indo-Gangetic plains, Central India, and Peninsular India in the SAS. Over the WCA and northern SAS, the blocking highs disrupt the north-westerly airmass intrusions, leading to sustained warm air advection (Satyanarayana and Rao 2020). We observe a significant north-westerly wind movement (Figure 9a) towards the central part of the SAS, which causes the advection of warm air from extremely hot northwest desert regions. This resulted in elevated temperatures, particularly in the north-western SAS and across rest of the region (Figure 9a), which is in agreement with the earlier studies (Satyanarayana and Rao 2020). The intense HHWs are possibly a result of the sinking air due to an upper atmospheric high over the northern SAS and subsequently warm air advection over the Indo-Gangetic plains, encompassing northern and eastern India, eastern Pakistan, southern Nepal, and Bangladesh in the SAS (Dubey et al. 2021b). This significant wind movement is absent during the non-HHW days (Figure 9b). This pattern is also evident in EH_x (Figures S14a, b). During HHW days, the difference (TW2 versus TW1) in composite specific humidity anomalies for ET_x^w (Figure 9c) and EH_x (Figure S14c) show a notable increase, particularly over the southern coastal SAS. While specific humidity rises from TW1 to TW2 during both HHW and non-HHW days (ET_x^w: Figure 9d; EH_x: Figure S14d), the increase is less pronounced during HHW days. This is because circulation patterns associated with HHWs, *e.g.*, persistent ridging/blocking often induce subsidence and strong daytime heating, which deepen the boundary-layer. Additionally, dry soil conditions can suppress evaporative cooling (Hanf et al. 2017; Wouters et al. 2022a), collectively resulting in a modest reduction in near-surface humidity anomalies during the HHWs. Despite this, the moisture anomaly remains positive and high, in particular near the coastal SAS, elevating the humid-heat stress (Figure 9c; Figure S14c). Furthermore, over the SAS, the negative OLR anomalies dominate during the HHW days (Figures 9e, S14e) in TW2, indicating that recent period (TW2) is characterized by more moisture dominated and cloud-influenced radiative state than the retrospective (TW1) period over the SAS. The difference in composite anomalies of the total cloud cover (TCC) shows spatially extensive positive anomalies over the SAS during the HHW days (Figures 9g, S14g),

which are stronger than those during non-HHW days (Figures 9h, S14h). The enhanced TCC corresponds to reduced OLR, indicating a decline in terrestrial heat loss to space and suppressed night-time cooling (Trenberth et al. 2015; Pyrgou et al. 2019). This phenomenon leads to a notable rise in humid heatwave conditions over western, central, and southern India, resulting in higher surface temperatures (Neethu and Abish 2025). The difference in the composite anomaly of sensible heat flux (SHF) shows a stronger sensible heating during the HHW days (Figures 9k, S14k) over the SAS, while the latent heat flux (LHF) changes are comparatively weaker (Figures 9i, S14i). For the LHF (Figure 9i: during HHW; 9j: without HHW), much of the SAS and adjoining northern Indian Ocean shows near-neutral to modestly negative differences, indicating little to no enhancement of evaporative cooling in TW2 relative to TW1 during HHW days (Figures 9i, S14i). In contrast, the SHF shows a pronounced and spatially coherent increase (Figures 9k, S14k) over the Indo-Gangetic plains and much of peninsular India, with a larger magnitude during HHW days (Figures 9k, S14k) compared to non-HHW days (Figures 9l, S14l). The positive SHF anomalies are observed over northern Pakistan, northern and the coastal India, and the Tibetan Plateau, indicating a spatial trend towards increase in moist heatwaves in recent times, which is in agreement with the literature (Banerjee et al. 2025).

Across the MENA, the difference in composite anomaly of geopotential heights (Figures 9a, S14a) during HHW days highlights strong positive anomalies over the MED, North Africa, the ARP, and WCA, indicating expansion and intensification of the subtropical highs and the development of blocking highs, conditions favoring extreme HHWs. Statistically significant wind anomalies over the land suggest the large-scale circulation changes can weaken monsoonal flows in Africa, promoting anticyclonic blocking over the ARP (Figures 9a, S14a) . This, in turn, favors warm-air advection into the MED, which subsequently extends toward the WCA and the northern subtropical belt, spanning from 30°N towards 50°N (Satyanarayana and Rao 2020). The weakly negative values of geopotential height anomalies over the CAF and SEAF, are likely due to the absence of significant blocking near the tropics. The difference in specific humidity anomaly of TW2 versus TW1 during HHW days (Figure 9c, S14c) portrays increase in atmospheric moisture during HHW days in recent times, particularly over Sahel (15.3°–26° N and 2° – 28° E), and south-western ARP and CAF. This elevated specific humidity in TW2 over the MED, SAH, and WAF regions is due to the large-scale moisture transport mechanisms. The warm sea surface temperature (SST) from moisture-rich sources, *e.g.*, the Gulf of Guinea, the Arabian Gulf, and the Red Sea, contributes to warm air advection inland (Zittis et al. 2022), resulting in greater heat accumulation during heatwave events (Zittis et al. 2016). Over the Persian Gulf (Figures 9a, S14a), anticyclonic subsidence promotes the development of a steep vertical moisture gradient. This pattern is consistent with an earlier assessment (Raymond et al. 2024), which documented a shallow, moist boundary layer overlaid by a markedly drier troposphere. Furthermore, over the MENA, the difference in composite anomaly signals is more spatially heterogeneous, but a distinct pattern emerges between interior desert zones and moisture-influenced coastal and near-coastal regions. During

HHW days, parts of North Africa and subtropical MED regions show positive OLR anomalies (Figures 9e, S14e), concurrent with negative TCC differences (Figures 9g, S14g), indicating reduced cloud cover, enhanced surface radiative heating (higher OLR), and a transition toward clear-sky, subsidence-dominated conditions in TW2. This behavior aligns with the established understanding that heat extremes in MENA during summer are often characterized by large-scale subsidence and cloud-free hot conditions as shown in earlier studies (Tyrlis et al. 2013; Lelieveld et al. 2016). During HHW days, the LHF anomalies for both ET_x^w (Figure 9i) and EH_x (Figure S14i) show only the modest increases over arid land surfaces, including North Africa, the Gulf region and WCA, with localized positive anomalies primarily along the Mediterranean rim and coastal zones. This pattern indicates that over MENA, the recent period does not show a pronounced enhancement in surface evaporation relative to the retrospective period. This phenomenon can be attributed to the air-sea heat flux change in the Mediterranean Sea (Paredes-Fortuny et al. 2025) or surface heat flux variations (Ghandy et al. 2025). However, during HHW days, the central ARP shows a modest increase in LHF (ET_x^w: Figure 9j and EH_x: Figure S14j), as compared to the non-HHW days (ET_x^w: Fig. 9j; EH_x: Figure S14j). The SHF anomalies (Figure 9k–l, S14 k-l) are spatially heterogeneous, with modest increases over the northern subtropical belt and parts of WCA, but predominantly show a decrease in the TW2 as compared to TW1. Taken together, unlike over SAS, the weakened SHF, contrasted by enhanced LHF over the Mediterranean in TW2, supports a transition toward a more evaporative, moisture-driven marine boundary layer. This can amplify coastal humid heatwave over the MENA when advected inland under persistent subtropical ridge conditions.

4. Summary and Conclusions

HHWs have emerged as the catastrophic climate hazards, particularly due to their combined thermal and physiological impacts (Baldwin et al. 2023). Extreme heat has already claimed over 2.6 million lives globally since the 2000s, underscoring the urgent need to understand and monitor compound heat extremes (Matthews 2025). Despite the SAS and MENA being among the most vulnerable regions experiencing HHWs, (Im et al. 2017; Saeed et al. 2021; Zittis et al. 2021; Guigma et al. 2021), a comprehensive assessment of HHW frequency, intensification, and spatiotemporal compounding remains limited over these regions. In our analysis, we systematically assess shifts in daily maximum heat−humidity metrics (wet-bulb temperature and extended heat index) versus derived extreme events from these metrics across the heatwave vulnerable regions of the SAS and MENA during the summer (March−August) based on in-situ observational data over two distinct periods (TW1: 1980–2000; TW2: 2001–2024). We observe a disparate trend in heat−humidity metrics in characterizing extreme HHW characteristics, which is potentially due to the relatively higher sensitivity of H_x to humidity compared to T_x^w (Rachid and Qureshi 2023). Understanding observed trends through extreme indices offers robust insights into future regional and global climate shifts. This study provides vital benchmarks for climate research, for example, climate model evaluation studies and climate impact adaptations. Our results indicate that both SAS and MENA have experienced a

widespread upward shift in daily heat–humidity conditions since 2000, but the translation of this background shift into extreme-event severity is spatially heterogeneous. Below we summarize the key region-specific implications:

- SAS shows a widespread intensification of the daily heat stress, with significant increase in the at-site median daily humid heatwave magnitude across approximately 80–90% of sites, together with increased autocorrelation at approximately 60–80% of sites, indicating temporal clustering of daily heat stress. In contrast, extreme HHW severity strengthens more locally, with only approximately 5–20% of sites displaying a significant rise in median HWMId. However, higher-order characteristics, i.e., skewness show an increase across approximately 60–70% of sites, while inter-arrival times significantly shortens across approximately 20–30% of sites, indicating rare and extreme HHWs tend to become frequent, occurring in close temporal succession. These results suggest that only median-based diagnostics alone may underestimate evolving HHW risk. Large-scale atmospheric patterns during record HHW days in the post-2000s reveal stronger mid-tropospheric ridging and blocking with coherent wind anomalies that favour north-westerly warm-air advection into central SAS and the Indo-Gangetic plains. The radiative and surface-energy signals further indicate that reduced OLR and higher cloud cover, together with enhanced sensible heating and weak changes in latent heat flux, can suppress nocturnal cooling, while elevating extreme humid-heat stress across SAS region.

- Likewise, MENA show a significant upward trend in at-site median daily humid heatwave magnitude across 76-91% of sites for heat−humidity series, accompanied by increased autocorrelation across approximately 60-70% of sites. Extreme HHWs, display a localized intensification, with only approximately 15–20% of sites showing a significant increase in median heatwave severity. However, increase in skewness are observed at approximately 60-70% of sites, together with a significant decline in inter-arrival time at approximately 20–30% of sites, suggesting a tendency toward a more frequent extreme HHWs occurring in closer succession at such localized hotspots. During HHW days in the post-2000s, MENA experiences an intensification of subtropical highs and the development of blocking conditions, with coherent wind anomalies that favour extreme HHWs. Unlike SAS, MENA region displays a strong interior–coastal contrast, with subsidence-dominated interiors and moisture-influenced coastal zones. This contrast is associated with reduced sensible heating but enhanced latent heat fluxes, which may amplify HHWs when moisture is advected inland. This pattern prominent across MED and APR climate subregions of the MENA.

- Over approximately 12% of sites across SAS and MENA, show a significant joint trend in upward changes in HHW severity, accompanied by a downward trend in inter-arrival times, indicating record HHWs tend to show a significant shortening in successive

occurrences, resulting in greater cumulative impact of sequential HHWs in recent times (2001−2024). Among sites showing such joint trend, 60% of cities are spatially clustered near the coasts of the SAS regions, and MED and ARP of MENA region. In contrast, approximately 30% of sites exhibit a decreasing trend in HHW severity, accompanied by a significant increase in inter-arrival times, indicating a shift toward less intense and less frequent HHW conditions, with longer intervals between successive events. Such sites are clustered within the same climate regions identified earlier; however, ~50% of these cities are located inland, more than 100 km from the coast. This contrast indicates that coastal cities across these climate reference regions are more susceptible to humid heat stress than inland cities.

- At an event scale, both metrics highlight an intense localized nature of HHWs in 2001−2024, with ET_x^w showing a notable upward shift in most of the HHW attributes.

We observe strong upward trends in extreme heatwave attributes, *e.g.*, frequency, and spatial extents, and in particular, the higher-order statistical moments of the HHW magnitude, are substantially higher in the recent period (2001–2024) compared to the retrospective era (1980−2000). Our ground-based observational assessment showed a localized intense HHW pattern, especially across the central MED, coastal ARP, coastal SAS, and western WAF—experience elevated HHW severity. While our findings of intensified humid heat stress across the Africa and Arabian Peninsula agrees with Speizer et al. (2022), the latter failed to identify the intensified HHW trends in coastal WAF and south-eastern ARP coast (Refer to Figure 1b in Speizer et al. 2022). Since humid heat stress is highly localized in space and time, reanalysis records and climate model simulations often fail to capture the severity and timing (seasonality) of humid heat, especially in areas with rugged topography, such as at coasts and mountainous regions (Freychet et al. 2020). Using an observational framework, we confirm daily heat stress to event-scale intensification of heat−humidity metrics using two state-of-the-art indices and quantify shifts in higher-order statistical moments that detect localized spatiotemporal compounding of HHWs, often underrepresented in coarser re-analysis datasets, especially in coastal tropics. Further, for the first time, we detected a significant bivariate trend considering both heat−humidity metrics, depicted by increasing HHW severity and shortening of inter-arrival times — the specific trend is pronounced for sites within 50 km from the coast. Despite increasing trends in HHW magnitude at most sites in recent times, a few sites show decreasing trends. On an at-site scale, trends can be spatially heterogeneous due to local scale effects, owing to nonlinear and compound interaction of temperature and moisture (Wang et al. 2024), local topographical effects, *e.g.*, physiographical attributes of the area, and location of the area in relation to the mountain ridge may influences thermal stress (Krzysztof et al. 2021). Land–atmosphere processes (soil-moisture coupling), for example, persistent soil droughts, can reduce heatwaves, primarily through reduced surface evaporation and increased entrainment of dry air aloft (Wang et al. 2020; Wouters et al. 2022), yielding weak or negative trends of

HHW magnitude at some locations. As a future reseach direction, an in-depth analysis involving topographical relief, urban-morphology (Paula et al. 2025) and local-scale land-atmospheric interactions in driving of HHW magnitude may be required to decipher such changes.

Our ground-based assessment offers crucial insights into warming trends and shifts in regional atmospheric circulation pattern, providing a valuable benchmark for regional and global climate models, especially in addressing the challenges of credibly assessing joint trends in heat and humidity (Christensen et al. 1997; Raäisaänen 2007; Zhao et al. 2015; Simpson et al. 2024). The results presented here have important implications for regional planning and improved climate adaptation policy design, in particular for outdoor workers and aged populations (Parsons et al. 2022). While in this paper, we have specifically focused on the summer season; elevated heatwave frequency and severity can be observed in other seasons, such as spring and autumn (Jiang and Xu 2025). Future research will broaden the analysis by incorporating seasonal dynamics that shape extreme heatwaves and associated attributes in monsoon-dominated regions of the world.

Author Contributions PG led this research, SD and SRS performed the analysis with the input from PG. SD carry out most of the analysis, draw figures and wrote the initial draft of the manuscript. PG provided constructive suggestions for improving the quality of the manuscript and prepared the initial code scripts. All authors read and approved the submitted version of the manuscript.

Data Availability The dataset used in this study is publicly available. It can be obtained from https://www.metoffice.gov.uk/hadobs/hadisd/v320_2021f/download.html. The at-site hydrometric observations across the SAS region, particularly India, from the IMD's Data Supply Portal, (https://dsp.imdpune.gov.in/data_supply_service.php#procedure). Geopotential height, specific humidity and components of wind vector time series are downloaded from the European Centre for Medium-Range Weather Forecasts (ECMWF)'s ERA-Interim product https://cds.climate.copernicus.eu/datasets.

Funding S. Deb acknowledges the Ministry of Education, Government of India, for the doctoral fellowship at the Indian Institutes of Technology, Kharagpur (IIT-KGP). S. R. Sherke is an undergraduate student and a recipient of the Chanakya Undergraduate Fellowship, 2024. Dr. P. Ganguli is supported by the Indo-German Science and Technology Centre's WISER grant (Project ID: WISER 2022/PG/47/2023-24).

Declarations

Conflict of Interest: The authors declare no conflict of interest.

References

Aadhar S, Mishra V (2023) The 2022 mega heatwave in South Asia in the observed and projected future climate. Environ Res Lett 18:104011. https://doi.org/10.1088/1748-9326/acf778

Agarwal S, Suchithra AS, Gurjar SP (2021) Analysis and Interpretation of Rainfall Trend using Mann-Kendall's and Sen's Slope Method. Indian J Ecol 48:453–457

Baldwin JW, Benmarhnia T, Ebi KL, et al (2023) Humidity's Role in Heat-Related Health Outcomes: A Heated Debate. Environ Health Perspect 131:055001. https://doi.org/10.1289/EHP11807

Baldwin JW, Dessy JB, Vecchi GA, Oppenheimer M (2019) Temporally Compound Heat Wave Events and Global Warming: An Emerging Hazard. Earths Future 7:411–427. https://doi.org/10.1029/2018EF000989

Banerjee A, Gupta S, Priyanshu P, et al (2025) Recent changes in spatiotemporal patterns of heat extremes in South Asia. Npj Clim Atmospheric Sci 8:293. https://doi.org/10.1038/s41612-025-01146-1

Birch CE, Jackson LS, Finney DL, et al (2022) Future Changes in African Heatwaves and Their Drivers at the Convective Scale. https://doi.org/10.1175/JCLI-D-21-0790.1

Brown SJ, Caesar J, Ferro C a. T (2008) Global changes in extreme daily temperature since 1950. J Geophys Res Atmospheres 113:. https://doi.org/10.1029/2006JD008091

Buzan JR, Huber M (2020) Moist Heat Stress on a Hotter Earth. Annu Rev Earth Planet Sci 48:623–655. https://doi.org/10.1146/annurev-earth-053018-060100

Christensen JH, Machenhauer B, Jones RG, et al (1997) Validation of present-day regional climate simulations over Europe: LAM simulations with observed boundary conditions. Clim Dyn 13:489–506. https://doi.org/10.1007/s003820050178

Dajuma A, Sylla MB, Tall M, et al (2024) Projected Intensification and Expansion of Heat Stress and Related Population Exposure Over Africa Under Future Climates. Earths Future 12:e2024EF004646. https://doi.org/10.1029/2024EF004646

de Bont J, Nori-Sarma A, Stafoggia M, et al (2024) Impact of heatwaves on all-cause mortality in India: A comprehensive multi-city study. Environ Int 184:108461. https://doi.org/10.1016/j.envint.2024.108461

Deb S, Raut A, Ganguli P (2025) Understanding Observed Trends in Moist Heatwaves in Urban Areas of South Asia and Middle East and North Africa (MENA) Regions. In: Das J, Umamahesh NV, Pu JH, Pandey M (eds) Climate Change Impact on Water Resources. Springer Nature, Singapore, pp 357–371

Devi R, Gouda KC, Lenka S (2023) Analysis of heat wave over different physiographical regions in India. Theor Appl Climatol 154:1343–1356. https://doi.org/10.1007/s00704-023-04639-2

Dhinakaran A (2023) How to Understand and Use the Jensen-Shannon Divergence. In: Medium. https://towardsdatascience.com/how-to-understand-and-use-jensen-shannon-divergence-b10e11b03fd6. Accessed 2 Aug 2024

Di Cecco GJ, Gouhier TC (2018) Increased spatial and temporal autocorrelation of temperature under climate change. Sci Rep 8:14850. https://doi.org/10.1038/s41598-018-33217-0

Donat MG, Alexander LV (2012) The shifting probability distribution of global daytime and night-time temperatures. Geophys Res Lett 39:. https://doi.org/10.1029/2012GL052459

Dong J, Brönnimann S, Hu T, et al (2024) Trends of the Intra-Annual Onset and End of Humid Heatwaves in the Northern Hemisphere. Earths Future 12:e2024EF005163. https://doi.org/10.1029/2024EF005163

Dubey AK, Kumar P, Saharwardi MS, Javed A (2021a) Understanding the hot season dynamics and variability across India. Weather Clim Extrem 32:100317. https://doi.org/10.1016/j.wace.2021.100317

Dubey AK, Kumar P, Saharwardi MS, Javed A (2021b) Understanding the hot season dynamics and variability across India. Weather Clim Extrem 32:100317. https://doi.org/10.1016/j.wace.2021.100317

Dunn RJH, Willett KM, Parker DE, Mitchell L (2016) Expanding HadISD: quality-controlled, sub-daily station data from 1931. Geosci Instrum Methods Data Syst 5:473–491. https://doi.org/10.5194/gi-5-473-2016

Dunn RJH, Willett KM, Thorne PW, et al (2012) HadISD: a quality-controlled global synoptic report database for selected variables at long-term stations from 1973–2011. Clim Past 8:1649–1679. https://doi.org/10.5194/cp-8-1649-2012

Engdaw MM, Ballinger AP, Hegerl GC, Steiner AK (2022) Changes in temperature and heat waves over Africa using observational and reanalysis data sets. Int J Climatol 42:1165–1180. https://doi.org/10.1002/joc.7295

Feron S, Cordero RR, Damiani A, et al (2019) Observations and Projections of Heat Waves in South America. Sci Rep 9:8173. https://doi.org/10.1038/s41598-019-44614-4

Freychet N, Hegerl G, Mitchell D, Collins M (2021) Future changes in the frequency of temperature extremes may be underestimated in tropical and subtropical regions. Commun Earth Environ 2:1–8. https://doi.org/10.1038/s43247-021-00094-x

Freychet N, Tett S f. b., Yan Z, Li Z (2020) Underestimated Change of Wet-Bulb Temperatures Over East and South China. Geophys Res Lett 47:e2019GL086140. https://doi.org/10.1029/2019GL086140

Ganguli P, Ganguly AR Robustness of Meteorological Droughts in Dynamically Downscaled Climate Simulations

Gedefaw M (2023) Assessment of changes in climate extremes of temperature over Ethiopia. Cogent Eng 10:2178117. https://doi.org/10.1080/23311916.2023.2178117

Ghandy R, Bidokhti AAA, Irannejad P, Ezam M (2025) Comprehensive analysis of air-sea interactions and surface heat fluxes in the Persian Gulf, Gulf of Oman, and Arabian Sea. Reg Stud Mar Sci 92:104633. https://doi.org/10.1016/j.rsma.2025.104633

Ghatak D, Zaitchik B, Hain C, Anderson M (2017) The role of local heating in the 2015 Indian Heat Wave. Sci Rep 7:7707. https://doi.org/10.1038/s41598-017-07956-5

Godard O (2008) The Stern Review on the Economics of Climate Change: contents, insights and assessment of the critical debate. SAPIENS Surv Perspect Integrating Environ Soc

Gramling C (2022) Heat waves appear more life-threatening than scientists once thought. https://www.snexplores.org/article/heat-waves-appear-more-life-threatening-than-scientists-once-thought. Accessed 16 July 2024

Guigma KH, MacLeod D, Todd M, Wang Y (2021) Prediction skill of Sahelian heatwaves out to subseasonal lead times and importance of atmospheric tropical modes of variability. Clim Dyn 57:537–556. https://doi.org/10.1007/s00382-021-05726-8

Ha K-J, Seo Y-W, Yeo J-H, et al (2022) Dynamics and characteristics of dry and moist heatwaves over East Asia. Npj Clim Atmospheric Sci 5:1–11. https://doi.org/10.1038/s41612-022-00272-4

Hajat S, Proestos Y, Araya-Lopez J-L, et al (2023a) Current and future trends in heat-related mortality in the MENA region: a health impact assessment with bias-adjusted statistically downscaled CMIP6 (SSP-based) data and Bayesian inference. Lancet Planet Health 7:e282–e290. https://doi.org/10.1016/S2542-5196(23)00045-1

Hajat S, Proestos Y, Araya-Lopez J-L, et al (2023b) Current and future trends in heat-related mortality in the MENA region: a health impact assessment with bias-adjusted statistically downscaled CMIP6 (SSP-based) data and Bayesian inference. Lancet Planet Health 7:e282–e290. https://doi.org/10.1016/S2542-5196(23)00045-1

Hamed MM, Al-Hasani AAJ, Nashwan MS, et al (2024) Assessing the growing threat of heat stress in the North Africa and Arabian Peninsula region connected to climate change. J Clean Prod 447:141639. https://doi.org/10.1016/j.jclepro.2024.141639

Hanf FS, Annamalai H, Rinke A, Dethloff K (2017) South Asian summer monsoon breaks: Process-based diagnostics in HIRHAM5. J Geophys Res Atmospheres 122:4880–4902. https://doi.org/10.1002/2016JD025967

Hu L (2021) A Global Assessment of Coastal Marine Heatwaves and Their Relation With Coastal Urban Thermal Changes. Geophys Res Lett 48:e2021GL093260. https://doi.org/10.1029/2021GL093260

Im E-S, Pal JS, Eltahir EAB (2017) Deadly heat waves projected in the densely populated agricultural regions of South Asia. Sci Adv 3:e1603322. https://doi.org/10.1126/sciadv.1603322

Intergovernmental Panel on Climate Change (IPCC) (ed) (2023) Weather and Climate Extreme Events in a Changing Climate. In: Climate Change 2021 – The Physical Science Basis: Working Group I Contribution to the Sixth Assessment Report of the Intergovernmental Panel on Climate Change. Cambridge University Press, Cambridge, pp 1513–1766

Iturbide M, Gutiérrez JM, Alves LM, et al (2020) An update of IPCC climate reference regions for subcontinental analysis of climate model data: definition and aggregated datasets. Earth Syst Sci Data 12:2959–2970. https://doi.org/10.5194/essd-12-2959-2020

Ivanovich C, Anderson W, Horton R, et al (2022) The Influence of Intraseasonal Oscillations on Humid Heat in the Persian Gulf and South Asia. https://doi.org/10.1175/JCLI-D-21-0488.1

Jackson LS, Birch CE, Chagnaud G, et al (2025) Daily rainfall variability controls humid heatwaves in the global tropics and subtropics. Nat Commun 16:3461. https://doi.org/10.1038/s41467-025-58694-6

Javed BDS (2023) Climate Change Made Asia Humid Heatwaves 30 Times More Likely : Attribution Study. In: Indian PSU Public Sect. Undert. News. https://indianpsu.com/climate-change-made-asia-humid-heatwaves-30-times-more-likely-attribution-study/. Accessed 15 Nov 2024

Jiang L, Xu R (2025) A new understanding of global heatwave characteristics: trends on trial and beyond summer scorch. Environ Res Lett 20:064040. https://doi.org/10.1088/1748-9326/addb61

Justine J, Monteiro JM, Shah H, Rao N (2023) The diurnal variation of wet bulb temperatures and exceedance of physiological thresholds relevant to human health in South Asia. Commun Earth Environ 4:244. https://doi.org/10.1038/s43247-023-00897-0

Kim Y-H, Min S-K, Zhang X, et al (2016) Attribution of extreme temperature changes during 1951–2010. Clim Dyn 46:1769–1782. https://doi.org/10.1007/s00382-015-2674-2

Kjellstrom T, Holmer I, Lemke B (2009) Workplace heat stress, health and productivity – an increasing challenge for low and middle-income countries during climate change. Glob Health Action 2:2047. https://doi.org/10.3402/gha.v2i0.2047

KNMI 2010 KNMI - 2000-2009, the warmest decade. https://www.knmi.nl/over-het-knmi/nieuws/2000-2009-the-warmest-decade. Accessed 16 Jan 2026

Kodra E, Ganguly AR (2014) Asymmetry of projected increases in extreme temperature distributions. Sci Rep 4:1–8. https://doi.org/10.1038/srep05884

Krzysztof B, Pavol N, Oleh S, et al (2021) Influence of geographical factors on thermal stress in northern Carpathians. Int J Biometeorol 65:1553–1566. https://doi.org/10.1007/s00484-020-02011-x

Lekshmi S, Chattopadhyay R, Pai DS (2026) Dynamics of Heat Wave Intensification over the Indian Region. https://doi.org/10.1175/JAS-D-24-0093.1

Lelieveld J, Proestos Y, Hadjinicolaou P, et al (2016) Strongly increasing heat extremes in the Middle East and North Africa (MENA) in the 21st century. Clim Change 137:245–260. https://doi.org/10.1007/s10584-016-1665-6

Lo S-H, Chen C-T, Russo S, et al (2021) Tracking heatwave extremes from an event perspective. Weather Clim Extrem 34:100371. https://doi.org/10.1016/j.wace.2021.100371

Lowe D, Ebi KL, Forsberg B (2011) Heatwave Early Warning Systems and Adaptation Advice to Reduce Human Health Consequences of Heatwaves. Int J Environ Res Public Health 8:4623–4648. https://doi.org/10.3390/ijerph8124623

Lu Y-C, Romps DM (2023) Predicting fatal heat and humidity using the heat index model. J Appl Physiol 134:649–656. https://doi.org/10.1152/japplphysiol.00417.2022

Malik A, Stenchikov G, Mostamandi S, et al (2024a) Accelerated Historical and Future Warming in the Middle East and North Africa. J Geophys Res Atmospheres 129:e2024JD041625. https://doi.org/10.1029/2024JD041625

Malik A, Stenchikov G, Mostamandi S, et al (2024b) Accelerated Historical and Future Warming in the Middle East and North Africa. J Geophys Res Atmospheres 129:e2024JD041625. https://doi.org/10.1029/2024JD041625

Marcotullio PJ, Keßler C, Fekete BM (2021) The future urban heat-wave challenge in Africa: Exploratory analysis. Glob Environ Change 66:102190. https://doi.org/10.1016/j.gloenvcha.2020.102190

Martinez-Villalobos C, Fu D, Loikith PC, Neelin JD (2025) Accelerating increase in the duration of heatwaves under global warming. Nat Geosci 18:716–723. https://doi.org/10.1038/s41561-025-01737-w

Matthews T (2018) Humid heat and climate change. Prog Phys Geogr Earth Environ 42:391–405. https://doi.org/10.1177/0309133318776490

Matthews T (2025) Mortality impacts of the most extreme heat events. Nat Rev Earth Environ 6:193–210. https://doi.org/10.1038/s43017-024-00635-w

Menéndez ML, Pardo JA, Pardo L, Pardo MC (1997) The Jensen-Shannon divergence. J Frankl Inst 334:307–318. https://doi.org/10.1016/S0016-0032(96)00063-4

Meque A, Pinto I, Maúre G, Beleza A (2022) Understanding the variability of heatwave characteristics in southern Africa. Weather Clim Extrem 38:100498. https://doi.org/10.1016/j.wace.2022.100498

Nairn J, Moise A, Ostendorf B (2022) The impact of humidity on Australia's operational heatwave services. Clim Serv 27:100315. https://doi.org/10.1016/j.cliser.2022.100315

NASA Earth Observatory, n.d. (2019) 2018 Was the Fourth Warmest Year, Continuing Long Warming Trend. In: NASA Earth Obs. Nd. https://earthobservatory.nasa.gov/images/144510/2018-was-the-fourth-warmest-year-continuing-long-warming-trend. Accessed 27 May 2025

Neethu CS, Abish B (2025) Climate variability and heat wave dynamics in India: Insights from land-atmospheric interactions. Dyn Atmospheres Oceans 110:101537. https://doi.org/10.1016/j.dynatmoce.2025.101537

New M, Hewitson B, Stephenson DB, et al (2006) Evidence of trends in daily climate extremes over southern and west Africa. J Geophys Res Atmospheres 111:. https://doi.org/10.1029/2005JD006289

Ngoungue Langue CG, Lavaysse C, Vrac M, Flamant C (2023) Heat wave monitoring over West African cities: uncertainties, characterization and recent trends. Nat Hazards Earth Syst Sci 23:1313–1333. https://doi.org/10.5194/nhess-23-1313-2023

Pal JS, Eltahir EAB (2016) Future temperature in southwest Asia projected to exceed a threshold for human adaptability. Nat Clim Change 6:197–200. https://doi.org/10.1038/nclimate2833

Paredes-Fortuny L, Pastor F, Khodayar S (2025) Concurrent atmospheric heatwaves intensify marine heatwaves through air-sea heat flux change in the Mediterranean Sea. Commun Earth Environ 6:638. https://doi.org/10.1038/s43247-025-02633-2

Parsons LA, Masuda YJ, Kroeger T, et al (2022) Global labor loss due to humid heat exposure underestimated for outdoor workers. Environ Res Lett 17:014050. https://doi.org/10.1088/1748-9326/ac3dae

Paula DCJ de, Valin Jr. MDO, Santos FMDM, et al (2025) The effects of urban morphology in a city with a tropical continental climate in the context of heat islands. Urban Clim 61:102381. https://doi.org/10.1016/j.uclim.2025.102381

Perkins SE, Alexander LV (2013) On the measurement of heat waves. J Clim 26:4500–4517. https://doi.org/10.1175/JCLI-D-12-00383.1

Perkins-Kirkpatrick SE, Gibson PB (2017) Changes in regional heatwave characteristics as a function of increasing global temperature. Sci Rep 7:12256. https://doi.org/10.1038/s41598-017-12520-2

Perkins-Kirkpatrick SE, Lewis SC (2020) Increasing trends in regional heatwaves. Nat Commun 11:3357. https://doi.org/10.1038/s41467-020-16970-7

Pyrgou A, Santamouris M, Livada I, et al (2019) Spatiotemporal Analysis of Diurnal Temperature Range: Effect of Urbanization, Cloud Cover, Solar Radiation, and Precipitation. Climate 7:. https://doi.org/10.3390/cli7070089

Raäisaänen J (2007) How reliable are climate models? Tellus Dyn Meteorol Oceanogr 59:2–29. https://doi.org/10.1111/j.1600-0870.2006.00211.x

Rachid A, Qureshi AM (2023) Sensitivity Analysis of Heat Stress Indices. Climate 11:181. https://doi.org/10.3390/cli11090181

Rashid I, Abid MA, Osman M, et al (2023) Predictability of the Early Summer Surface Air Temperature over Western South Asia

Raymond C (2025) cr2630git/wetbulb_dj08_spedup

Raymond C, Matthews T, Horton RM (2020) The emergence of heat and humidity too severe for human tolerance. Sci Adv 6:eaaw1838. https://doi.org/10.1126/sciadv.aaw1838

Raymond C, Matthews T, Tuholske C (2024a) Post-Sunset Humid-Heat Maxima near the Southern Persian/Arabian Gulf

Raymond C, Matthews T, Tuholske C (2024b) Evening humid-heat maxima near the southern Persian/Arabian Gulf. Commun Earth Environ 5:591. https://doi.org/10.1038/s43247-024-01763-3

Raymond C, Singh D, Horton RM (2017) Spatiotemporal Patterns and Synoptics of Extreme Wet-Bulb Temperature in the Contiguous United States. J Geophys Res Atmospheres 122:13,108-13,124. https://doi.org/10.1002/2017JD027140

Rogers CD, Warren RA (2024) Fast and Accurate Calculation of Wet-bulb Temperature for Humid-Heat Extremes. Authorea Prepr

Rogers CDW, Ting M, Li C, et al (2021) Recent Increases in Exposure to Extreme Humid-Heat Events Disproportionately Affect Populated Regions. Geophys Res Lett 48:e2021GL094183. https://doi.org/10.1029/2021GL094183

Rohini P, Rajeevan M, Srivastava AK (2016) On the Variability and Increasing Trends of Heat Waves over India. Sci Rep 6:26153. https://doi.org/10.1038/srep26153

Rothfusz LP, Headquarters NSR (1990) The heat index equation (or, more than you ever wanted to know about heat index). Ft Worth Tex Natl Ocean Atmospheric Adm Natl Weather Serv Off Meteorol 9023:640

Röthlisberger M, Papritz L (2023) Quantifying the physical processes leading to atmospheric hot extremes at a global scale. Nat Geosci 16:210–216. https://doi.org/10.1038/s41561-023-01126-1

Russo S, Dosio A, Graversen RG, et al (2014) Magnitude of extreme heat waves in present climate and their projection in a warming world. J Geophys Res Atmospheres 119:12,500-12,512. https://doi.org/10.1002/2014JD022098

Russo S, Marchese AF, Sillmann J, Immé G (2016) When will unusual heat waves become normal in a warming Africa? Environ Res Lett 11:054016. https://doi.org/10.1088/1748-9326/11/5/054016

Russo S, Sillmann J, Sterl A (2017) Humid heat waves at different warming levels. Sci Rep 7:1–7. https://doi.org/10.1038/s41598-017-07536-7

Saeed F, Schleussner C-F, Ashfaq M (2021) Deadly Heat Stress to Become Commonplace Across South Asia Already at 1.5°C of Global Warming. Geophys Res Lett 48:e2020GL091191. https://doi.org/10.1029/2020GL091191

Saha P, Mahanta R, Goswami BN (2023) Present and future of the South Asian summer monsoon's rainy season over Northeast India. Npj Clim Atmospheric Sci 6:170. https://doi.org/10.1038/s41612-023-00485-1

Saha P, Monteiro JM, Bora P, et al (2025) Heightened Adaptability Challenges from Extreme Humid Heat Stress for South Asia

Saleem F, Zeng X, Hina S, Omer A (2021) Regional changes in extreme temperature records over Pakistan and their relation to Pacific variability. Atmospheric Res 250:105407. https://doi.org/10.1016/j.atmosres.2020.105407

Satyanarayana G (2021) An accentuated "hot blob" over Vidarbha, India, during the pre-monsoon season. Nat Hazards 105:. https://doi.org/10.1007/s11069-020-04357-2

Satyanarayana GCh, Rao DVB (2020) Phenology of heat waves over India. Atmospheric Res 245:105078. https://doi.org/10.1016/j.atmosres.2020.105078

Schär C, Chiriatti F (2025) Revisiting recent changes in European summer temperature distributions and assessing their role for extreme summer temperatures. https://meetingorganizer.copernicus.org/EGU25/EGU25-17421.html

Shafiei Shiva J, Chandler DG, Kunkel KE (2019) Localized Changes in Heat Wave Properties Across the United States. Earths Future 7:300–319. https://doi.org/10.1029/2018EF001085

Simpson C, Hosking JS, Mitchell D, et al (2021) Regional disparities and seasonal differences in climate risk to rice labour. Environ Res Lett 16:124004. https://doi.org/10.1088/1748-9326/ac3288

Simpson IR, McKinnon KA, Kennedy D, et al (2024) Observed humidity trends in dry regions contradict climate models. Proc Natl Acad Sci 121:e2302480120. https://doi.org/10.1073/pnas.2302480120

Smith A, Lott N, Vose R (2011) The Integrated Surface Database: Recent Developments and Partnerships. Bull Am Meteorol Soc 92:704–708. https://doi.org/10.1175/2011BAMS3015.1

Speizer S, Raymond C, Ivanovich C, Horton RM (2022) Concentrated and Intensifying Humid Heat Extremes in the IPCC AR6 Regions. Geophys Res Lett 49:e2021GL097261. https://doi.org/10.1029/2021GL097261

Stephenson TS, Vincent LA, Allen T, et al (2014) Changes in extreme temperature and precipitation in the Caribbean region, 1961–2010. Int J Climatol 34:2957–2971. https://doi.org/10.1002/joc.3889

Tandon A (2024) Climate change made west Africa's 'dangerous humid heatwave' 10 times more likely. In: Carbon Brief. C. Accessed 17 July 2024

Trenberth KE, Zhang Y, Fasullo JT, Taguchi S (2015) Climate variability and relationships between top-of-atmosphere radiation and temperatures on Earth. J Geophys Res 120:3642–3659. https://doi.org/10.1002/2014JD022887

Tyrlis E, Lelieveld J, Steil B (2013) The summer circulation over the eastern Mediterranean and the Middle East: influence of the South Asian monsoon. Clim Dyn 40:1103–1123. https://doi.org/10.1007/s00382-012-1528-4

Uckan Y, Ruiz-Vásquez M, De Polt K, Orth R (2024) Global relevance of atmospheric and land surface drivers for hot temperature extremes. https://doi.org/10.5194/egusphere-2024-2540

UN U (2010) The past decade was the warmest on record, UN weather agency says | UN News. https://news.un.org/en/story/2010/03/333542. Accessed 19 Jan 2026

Van Oldenborgh GJ, Wehner MF, Vautard R, et al (2022) Attributing and Projecting Heatwaves Is Hard: We Can Do Better. Earths Future 10:e2021EF002271. https://doi.org/10.1029/2021EF002271

Varela R, Rodríguez-Díaz L, Barriopedro D, et al (2022) Projected changes in the season of hot days in the Middle East and North Africa. Int J Climatol 42:2195–2207. https://doi.org/10.1002/joc.7360

Varela R, Rodríguez-Díaz L, deCastro M (2020) Persistent heat waves projected for Middle East and North Africa by the end of the 21st century. PLOS ONE 15:e0242477. https://doi.org/10.1371/journal.pone.0242477

Vogel MM, Zscheischler J, Fischer EM, Seneviratne SI (2020) Development of Future Heatwaves for Different Hazard Thresholds. J Geophys Res Atmospheres 125:e2019JD032070. https://doi.org/10.1029/2019JD032070

Wang F, Gao M, Liu C, et al (2024) Uniformly elevated future heat stress in China driven by spatially heterogeneous water vapor changes. Nat Commun 15:4522. https://doi.org/10.1038/s41467-024-48895-w

Wang P, Tang J, Wang S, et al (2018) Regional heatwaves in china: a cluster analysis. Clim Dyn 50:1901–1917. https://doi.org/10.1007/s00382-017-3728-4

Wang P, Yang Y, Tang J, et al (2021) Intensified Humid Heat Events Under Global Warming. Geophys Res Lett 48:e2020GL091462. https://doi.org/10.1029/2020GL091462

Wang X, Liu H, Miao S, et al (2020) Effectiveness of Urban Hydrological Processes in Mitigating Urban Heat Island and Human Thermal Stress During a Heat Wave Event in Nanjing, China. J Geophys Res Atmospheres 125:e2020JD033275. https://doi.org/10.1029/2020JD033275

Wang X-S, He L, Ma X-H, et al (2022) The emergence of prolonged deadly humid heatwaves. Int J Climatol 42:8607–8618. https://doi.org/10.1002/joc.7750

Whan K, Alexander LV, Imielska A, et al (2014) Trends and variability of temperature extremes in the tropical Western Pacific. Int J Climatol 34:2585–2603. https://doi.org/10.1002/joc.3861

WMO (2025) Rising temperatures and extreme weather hit Asia hard. In: World Meteorol. Organ. https://wmo.int/news/media-centre/rising-temperatures-and-extreme-weather-hit-asia-hard. Accessed 6 July 2025

WMO (2022) Climate change made heatwaves in India and Pakistan "30 times more likely." https://public.wmo.int/en/media/news/climate-change-made-heatwaves-india-and-pakistan-30-times-more-likely. Accessed 31 July 2023

Wouters H, Keune J, Petrova IY, et al (2022a) Soil drought can mitigate deadly heat stress thanks to a reduction of air humidity. Sci Adv 8:eabe6653. https://doi.org/10.1126/sciadv.abe6653

Wouters H, Keune J, Petrova IY, et al (2022b) Soil drought can mitigate deadly heat stress thanks to a reduction of air humidity. Sci Adv 8:eabe6653. https://doi.org/10.1126/sciadv.abe6653

Xie F, Nian D, Fu Z (2019a) Differential temporal asymmetry among different temperature variables' daily fluctuations. Clim Dyn 53:585–600. https://doi.org/10.1007/s00382-018-04603-1

Xie F, Nian D, Fu Z (2019b) Differential temporal asymmetry among different temperature variables' daily fluctuations. Clim Dyn 53:585–600. https://doi.org/10.1007/s00382-018-04603-1

Xu F, Chan TO, Luo M (2021) Different changes in dry and humid heat waves over China. Int J Climatol 41:1369–1382. https://doi.org/10.1002/joc.6815

Ye H, Fetzer EJ (2019) Asymmetrical Shift Toward Longer Dry Spells Associated with Warming Temperatures During Russian Summers. Geophys Res Lett 46:11455–11462. https://doi.org/10.1029/2019GL084748

Ye J, Xiao C, Esteves R, Rong C (2015) Time Series Similarity Evaluation Based on Spearman's Correlation Coefficients and Distance Measures

Zhang L, Jiapaer G, Yu T, et al (2024) Evaluating and Correcting Temperature and Precipitation Grid Products in the Arid Region of Altay, China. Remote Sens 16:283. https://doi.org/10.3390/rs16020283

Zhang X, Alexander L, Hegerl GC, et al (2011) Indices for monitoring changes in extremes based on daily temperature and precipitation data. WIREs Clim Change 2:851–870. https://doi.org/10.1002/wcc.147

Zhao Y, Ducharne A, Sultan B, et al (2015) Estimating heat stress from climate-based indicators: present-day biases and future spreads in the CMIP5 global climate model ensemble. Environ Res Lett 10:084013. https://doi.org/10.1088/1748-9326/10/8/084013

1053 Zhou Y, Ren G (2011) Change in extreme temperature event frequency over mainland China,
1054 1961−2008. Clim Res 50:125–139. https://doi.org/10.3354/cr01053
1055 Zittis G, Hadjinicolaou P, Almazroui M, et al (2021) Business-as-usual will lead to super and ultra-
1056 extreme heatwaves in the Middle East and North Africa. Npj Clim Atmospheric Sci 4:20
1057 Zittis G, Hadjinicolaou P, Fnais M, Lelieveld J (2016) Projected changes in heat wave characteristics
1058 in the eastern Mediterranean and the Middle East. Reg Environ Change 16:1863–1876.
1059 https://doi.org/10.1007/s10113-014-0753-2
1060 Zscheischler J, Martius O, Westra S, et al (2020) A typology of compound weather and climate events.
1061 Nat Rev Earth Environ 1:333–347. https://doi.org/10.1038/s43017-020-0060-z
1062

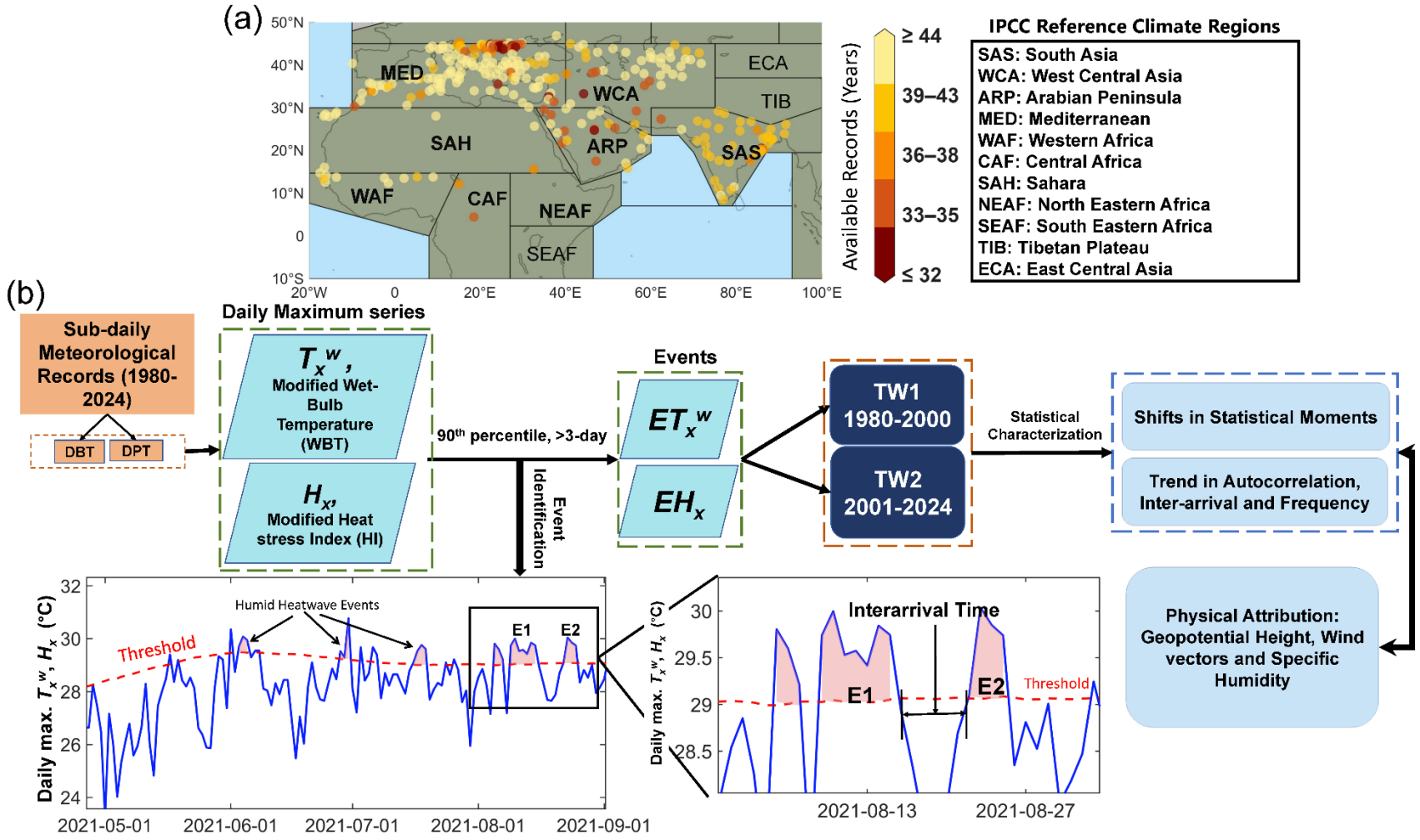

Figure 1. Description of study domain and workflow of overall analysis (a) Study area**.** Regions that are considered here are marked in bold characters**,** and **(b)** Schematic representation of the detailed workflow. The time frame to detect humid heatwaves for a representative site, Sriniketan (WMO ID 427080) in eastern part of the SAS, is marked using a rectangular box in solid black. We define an extreme humid heatwave (HHW) event when the daily maximum heat–humidity quantity (T_x^w and H_x values) time series (indicated in blue solid lines) exceed the daily

variable threshold of the 90th percentile (indicated by the red dashed line) and remain persistently above this threshold consecutively for more than three days or longer. For example, here, a six-day-long HHW event (E1) is detected starting on 09-08-2021 and ending on 15-08-2021, which is followed by a four-day-long HHW event, initiated on 22-08-2021 and terminated on 26-08-2021. The inter-arrival time is calculated as the number of days between the termination of E1 (15-08-2021) and the beginning of the next event (E2) on 22-08-2021. Thus, the inter-arrival time in this case is 8 days.

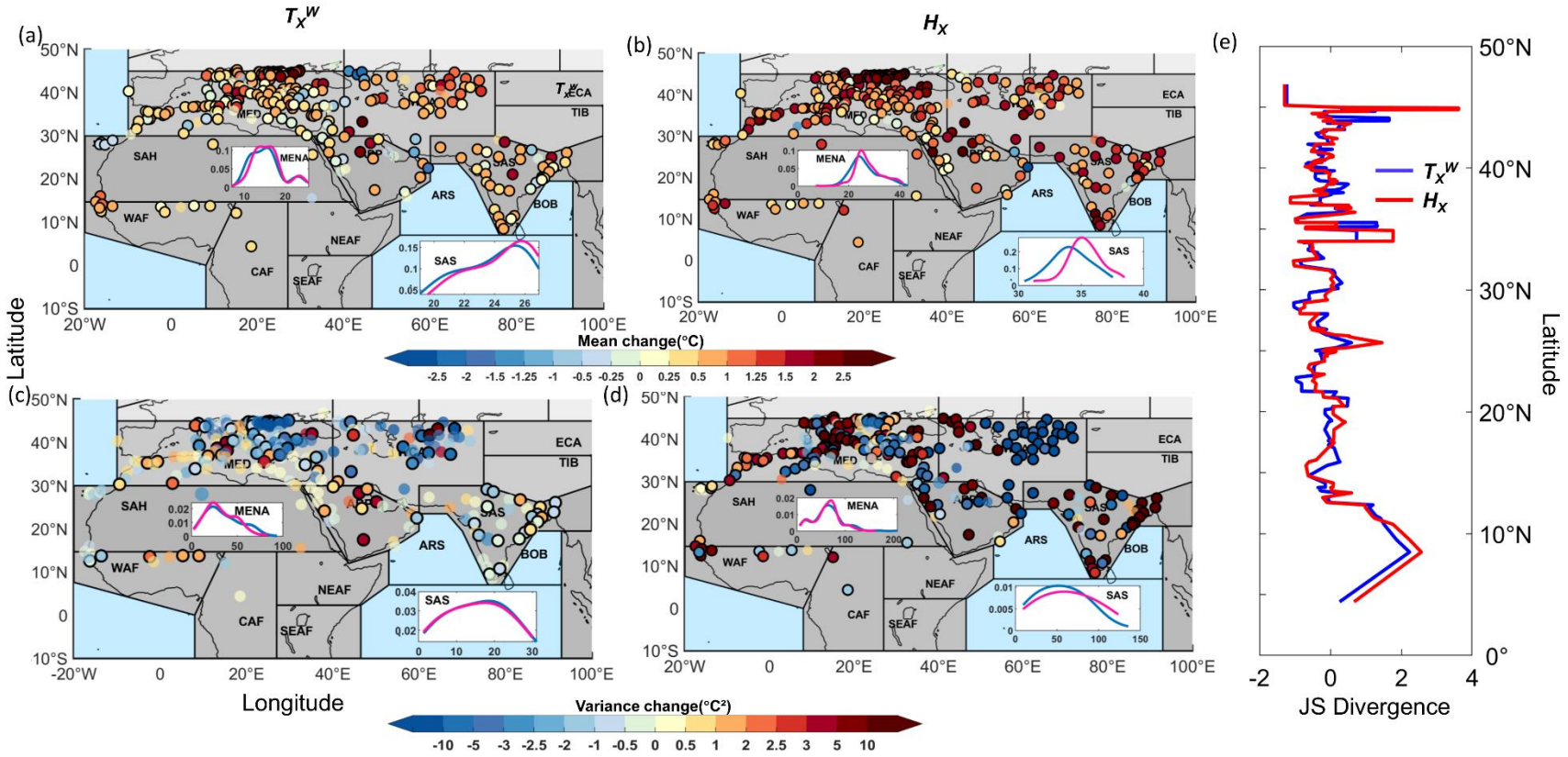

Figure 2. Shifts in daily heat–humidity time series over the recent (2001-2024) versus retrospective (1980-2000) time windows. The maps display the changes (2001−2024 versus 1980−2000) in median and variability in the daily series of **(a, c)** wet-bulb temperature series, T_x^w and **(b, d)** Extended heat index series, H_x series. The sites with significant at-site trends are marked in circles with black edge colors, whereas, sites with insignificant trends are shown with transparent shades with no solid edge colors. The sub-plots within the figures present the probability density function (PDFs) diagram comparing the frequency in the at-site magnitude of daily humid heat metrics events between the two-time windows (TW1: PDFs in blue and TW2: PDFs in pink). The density diagrams were determined using Kernel Density function. **(e)** Latitudinal transects comparing the JSDs of at-site T_x^w and H_x series during 1980-2024. The analysis of shifts in at-site median and variance are performed using the Wilcoxon rank-sum test and Levene's test, respectively, at a 10% significance level.

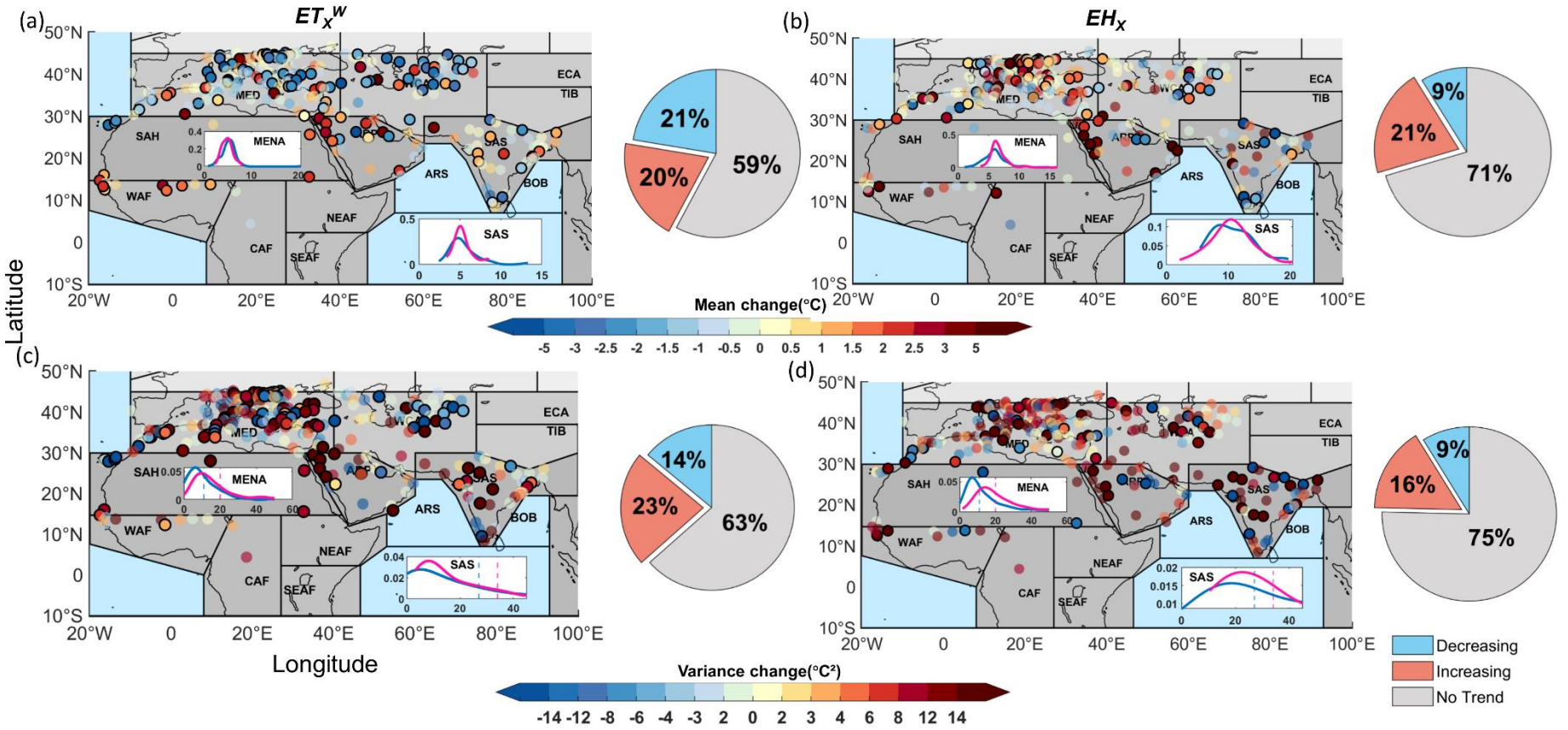

Figure 3. **Shifts in extreme HHW events over recent (2001-2024) versus retrospective (1980-2000) time windows.** The maps display the changes (2001−2024 versus 1980−2000) in median and variability of the heatwave magnitude (*i.e.*, severity), quantified by HWMId considering **(a, c)** ET_x^w and **(b, d)** EH_x, respectively. The sites with significant at-site trends are marked in circles with black edge color, whereas, sites with insignificant trends are shown with transparent shades with no solid edge color. The sub-plots present the PDFs comparing the frequency of the at-site HHW magnitudes between the two-time windows (TW1: PDFs in blue and TW2: PDFs in pink). The density diagrams were determined using Kernel Density function. The pie charts across the right column of each spatial map show the percentage share of sites with a significant increasing (or decreasing) and insignificant trends in HWMId for the respective heat−humidity metrics. The analysis of shifts in at-site median and variance is performed using the Wilcoxon rank sum test and Levene's test, respectively, at a 10% significance level.

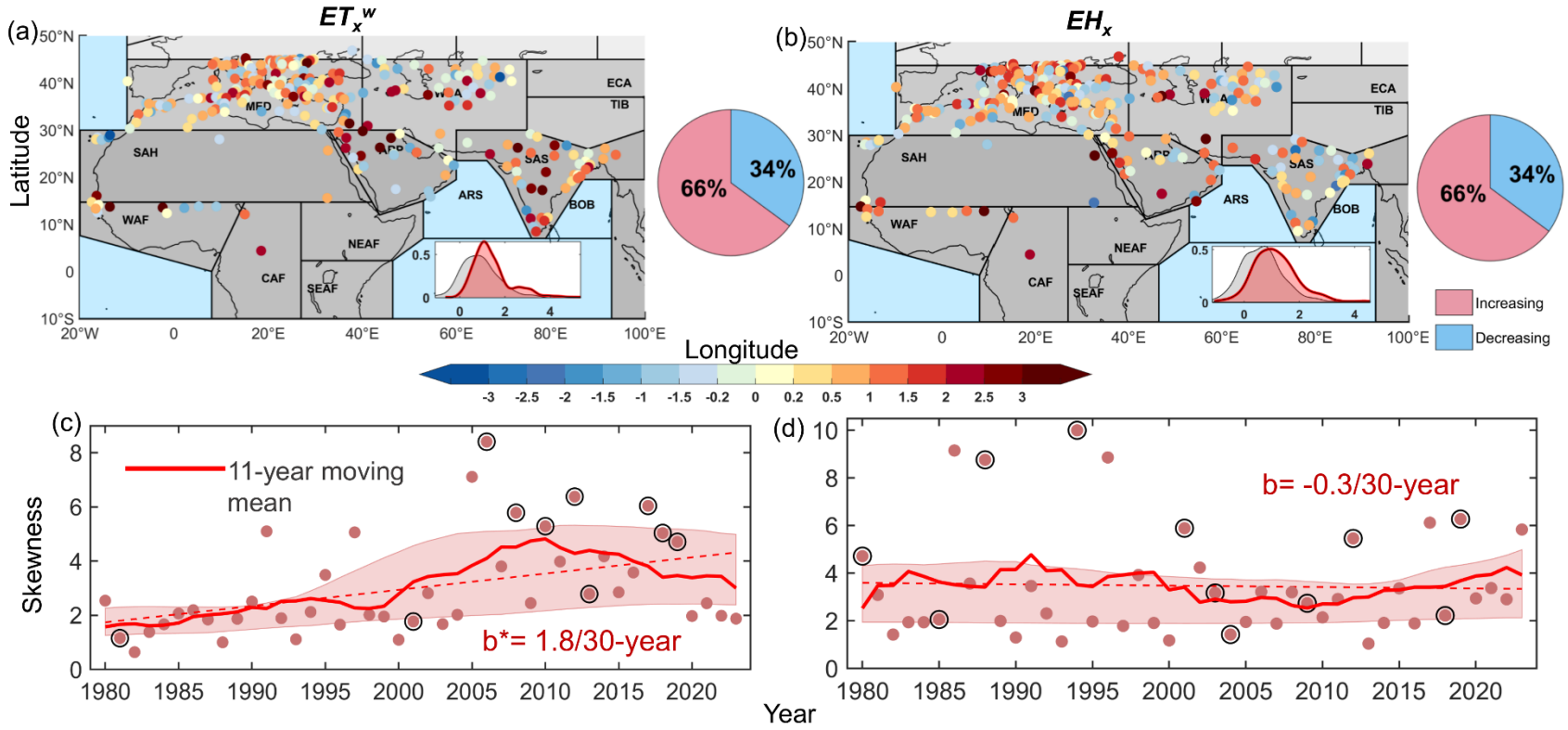

Figure 4. **Shifts in Skewness of the humid heatwave severity over recent (2001-2024) versus retrospective (1980-2000) time windows.** Spatial distributions of changes (2001−2024 versus 1980−2000) in at-site skewness of the HWMId considering **(a)** ET_x^w and **(b)** EH_x respectively. The sub-plots present the PDFs comparing the frequency of the at-site skewness values of the HWMId between the two-time windows (TW1: PDFs in grey and TW2: PDFs in red), which suggest an overall rightward shift in skewness in TW2, indicating severe HHWs tend to become more frequent than expected from the changes in median. The pie charts across the right column of each spatial map show the percentage share of sites with an increase (or a decrease) in skewness. **(c –d)** present the temporal evolution of annual skewness of HWMId from 1980 to 2023, for **(c)** ET_x^w and **(d)** EH_x, respectively. The annual skewness is smoothed using an 11-day moving average shown with a solid red curve. The shaded red envelope indicates the interquartile range (IQR), illustrating the range between the 25th and 75th percentiles. Years marked with black-edged circles correspond to warmest years with the highest HWMId. The trend lines (in dashed red) are fitted using the least-square regression fit. The statistical evaluations of trend significance is performed using the *F*-test at a 10% significance level. The significant slope changes are represented by *b**.

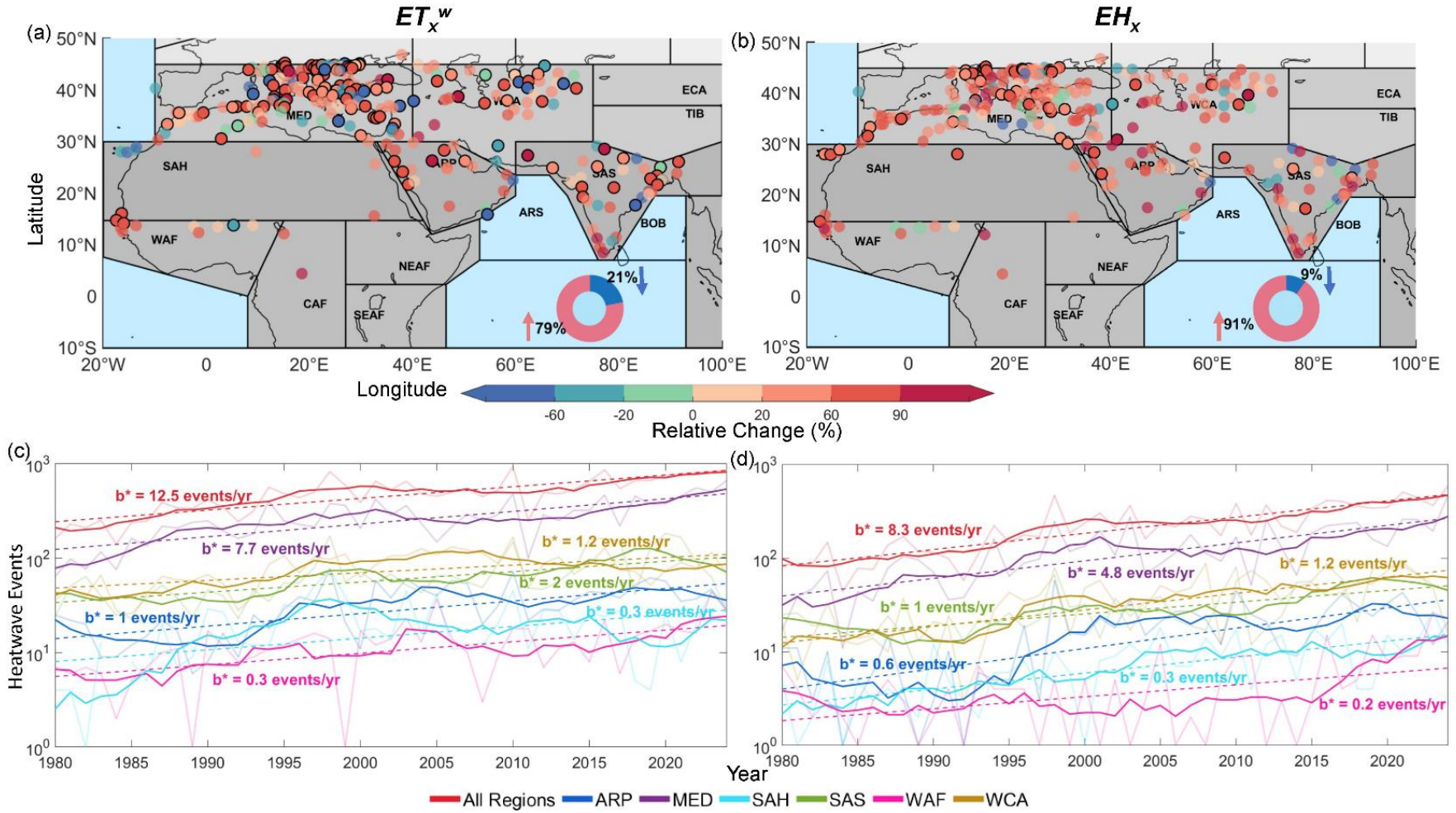

Figure 5. Trends in extreme HHW event frequency from 1980-2024. (a, b) Maps displaying the percentage changes in at-site HHW event frequency during the recent period (2001–2024) relative to the retrospective period (1980–2000), based on **(a)** ET_x^w and **(b)** EH_x. The sites with significant changes are marked in circles with black edge colors, whereas, sites with insignificant trend are shown with transparent shades. The statistical evaluation of changes in at-site event frequency is **(a, b)** performed using the Wilcoxon rank sum test at a 10% significance level. The inset donut charts display the proportion of sites exhibiting significantly increasing (red) and decreasing (blue) trends. **(c, d)** show trends in the frequency of HHW events (event counts/year), for **(c)** ET_x^w and **(d)** EH_x

respectively. The curves in shade show the absolute HHW event frequency during the summer season (March−August) reported for each year. The HHW frequency is smoothed using a 7-year moving average, shown with the solid lines of colors for all versus different regions. Trends in frequency is evaluated using the least-square linear regression fit, shown in dashed solid lines in **(c, d)**. The statistical evaluations of trend significance is performed using the *F*-test at a 10% significance level. The significant slope changes are represented by *b**.

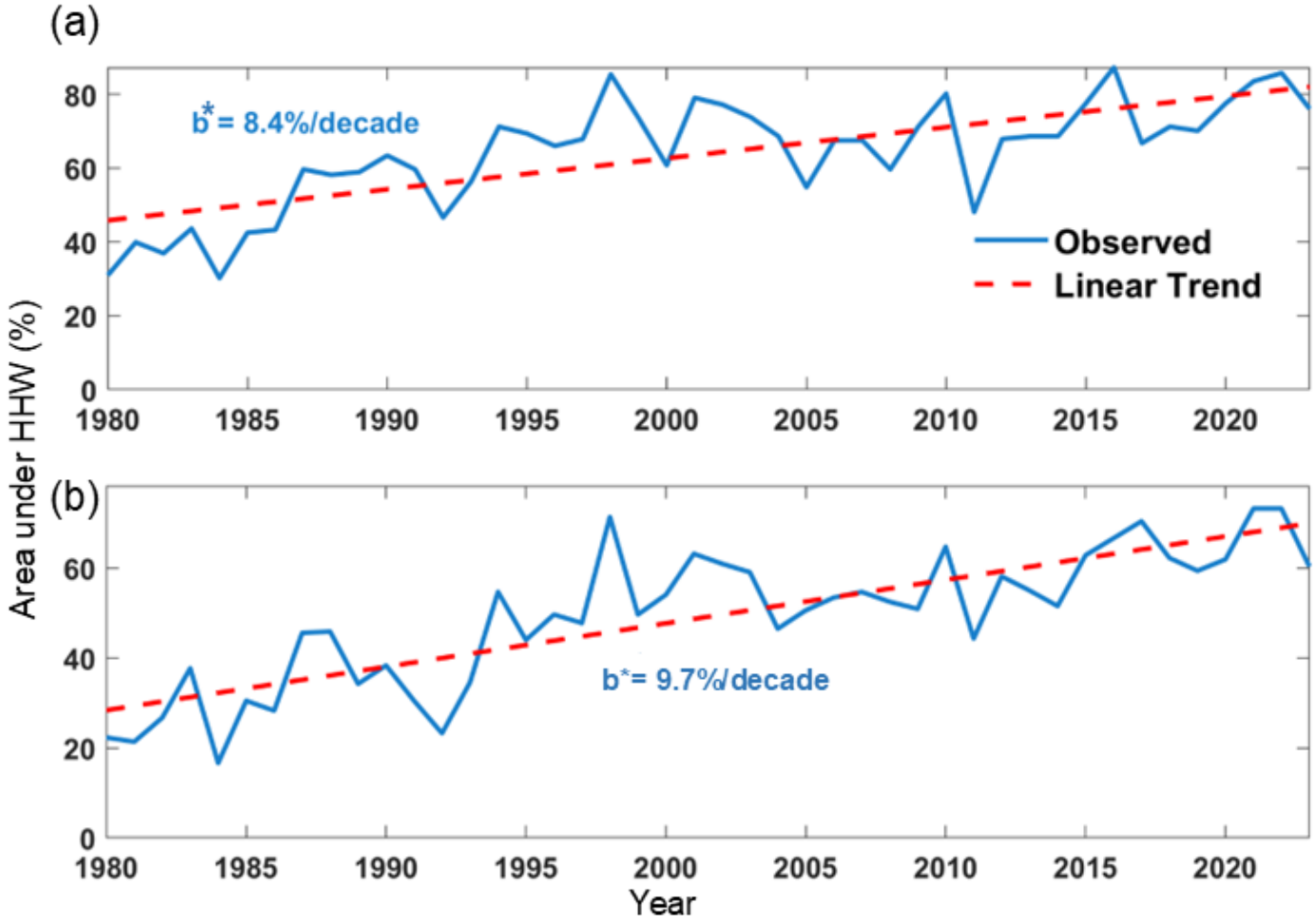

Figure 6. Areal coverage of HHWs in different years. Percentage of area affected by HHWs during 1980−2024 for **(a)** ET_x^w and **(b)** EH_x. The solid lines in blue represent the fraction of observed areal coverage of HHWs for each year. The trends lines are fitted using the least-square linear regression fit, shown using dashed lines in red. The statistical evaluation of trend significance is performed using the *F*-test. The significant slope changes are represented using *b**. Trends are statistically significant, with a *P*-value < 0.10.

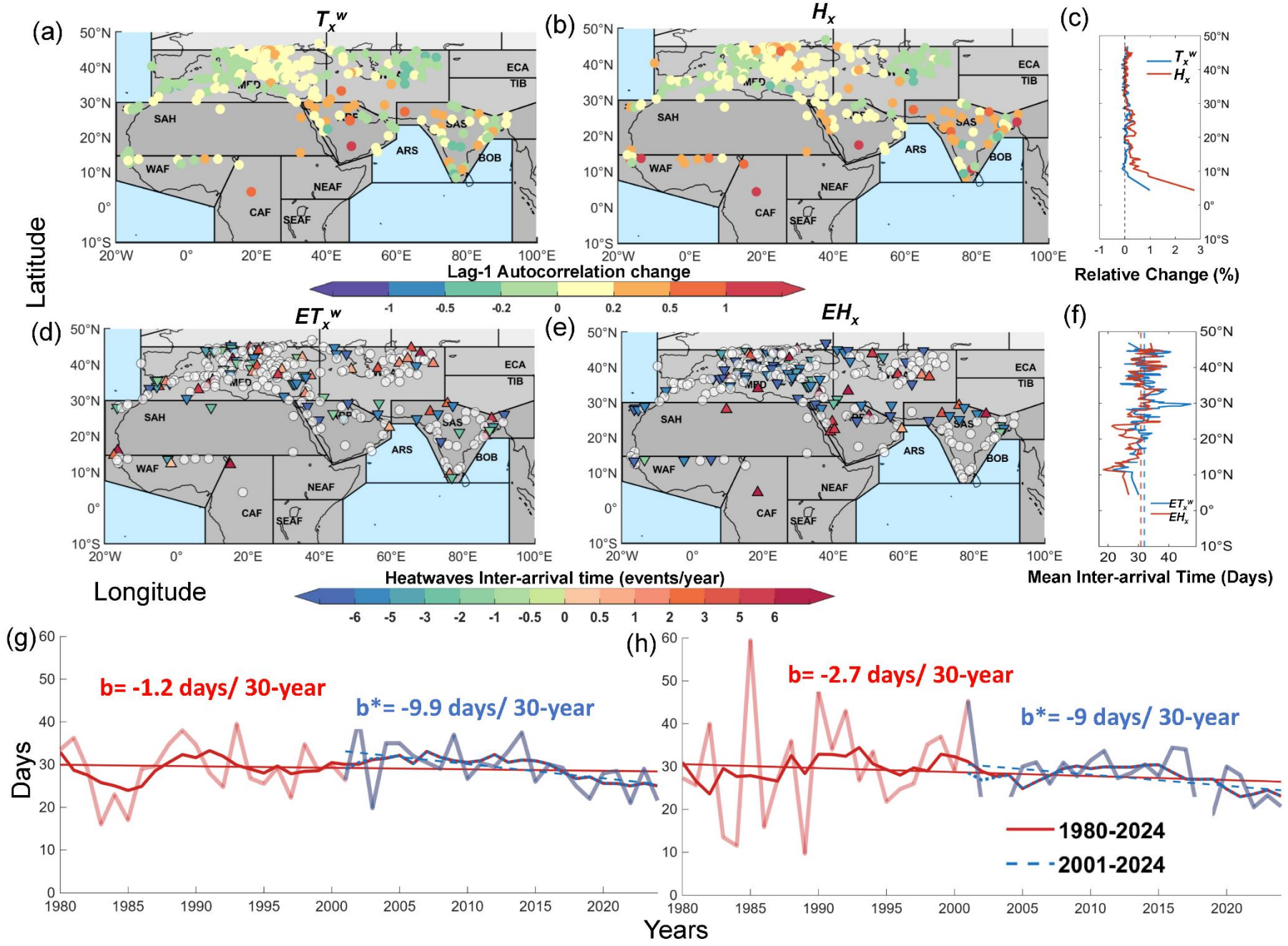

Figure 7. Changes in Lag-1 autocorrelation and trends in inter-arrival time of HHW events from 1980–2024. The maps displaying the absolute changes (2001−2024 versus 1980−2000) in lag-1 autocorrelation of **(a)** T_x^w and **(b)** H_x series, respectively **(c)** Latitudinal transects showing the relative changes (%) in lag-1 autocorrelation. Spatial distribution of changes (2001-2024 vs. 1980-2000) in inter-arrival times between two consecutive HHW events considering **(d)** ET_x^w and **(e)** EH_x, respectively. Statistical significance of changes in inter-arrival times was evaluated using $N = 5000$ bootstrap iterations at a 10% significance level. **(f)** Latitudinal transects showing the mean inter-arrival time (days). The vertical dashed lines in blue (ET_x^w) and red (EH_x) show the mean of the mean inter-arrival time (days). The site close to the equator (~ 0°N) shows a prominent increase in mean inter-arrival time, has disparate HHW event sample lengths *i.e.* 37 HHW events for ET_x^w and 15 HHW events for EH_x. **(g –h)** show trends in inter-arrival times from 1980 to 2024, for **(g)** ET_x^w and **(h)** EH_x, respectively. The inter-arrival times are smoothed using a 7-day moving average shown with a solid

curve. The trends in inter-arrival times are fitted using the least-square linear regression fit, shown using the solid lines, with slope (*b*) reporting the trend estimate. The statistical significance of trend estimates **(g, h)** are evaluated using the *F*-test at a 10% significance level. Significant slope changes are represented using *b**.

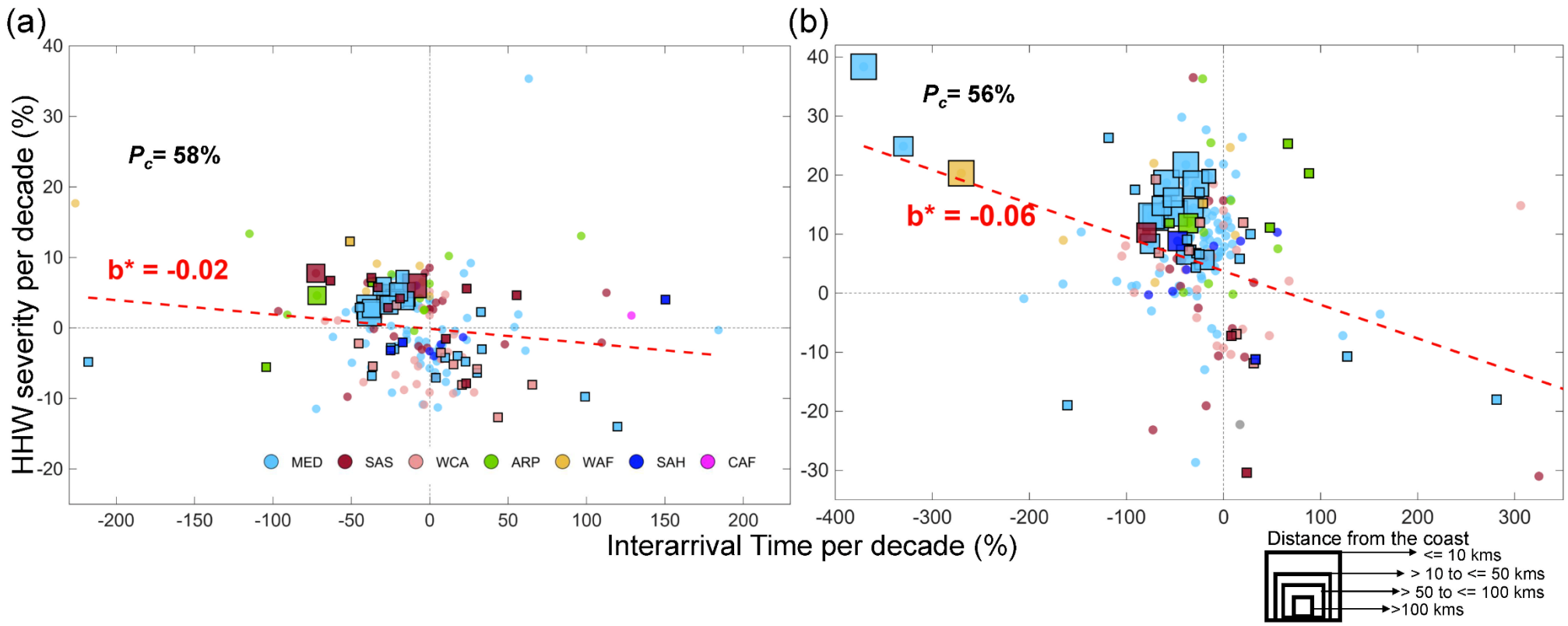

Figure 8. Scatter plots showing changes in HHW magnitude versus trend in inter-arrival Times. Scatter plots depicting the relationship between percentage shifts in HHW severity (HWMId) and inter-arrival times for **(a)** ET_x^w and **(b)** EH_x. The x-axis denotes the trend in inter-arrival time per decade (in %), while the y-axis indicates HHW severity magnitude per decade (in %). Trends are computed using the decadal changes of normalized Sen's slope (See SI S1.3 for details) at a 10% significance level. P_c indicates the percentage of sites that are located within 50-km from the coast out of all sites showing significant joint trends in increasing severity and shortening of inter-arrival times (those points fall in the 2nd quadrant). The markers are shaded by corresponding IPCC reference climate regions, as indicated in the legends. The marker in circle denotes a site with at least one of the attributes showing a significant trend, whereas the square markers with solid black edge color highlight sites with statistically significant trends in both attributes, with size indicating distance from the coast — bigger square indicate proximity to the coast, while a smaller sized marker indicate away from the coast (see legends in right corner). Trend in scatter plots is fitted using the least-square linear regression fit (shown using dashed lines in red). The trend significance is evaluated using the *F*-test at a 10% significance level and denoted by *b**.

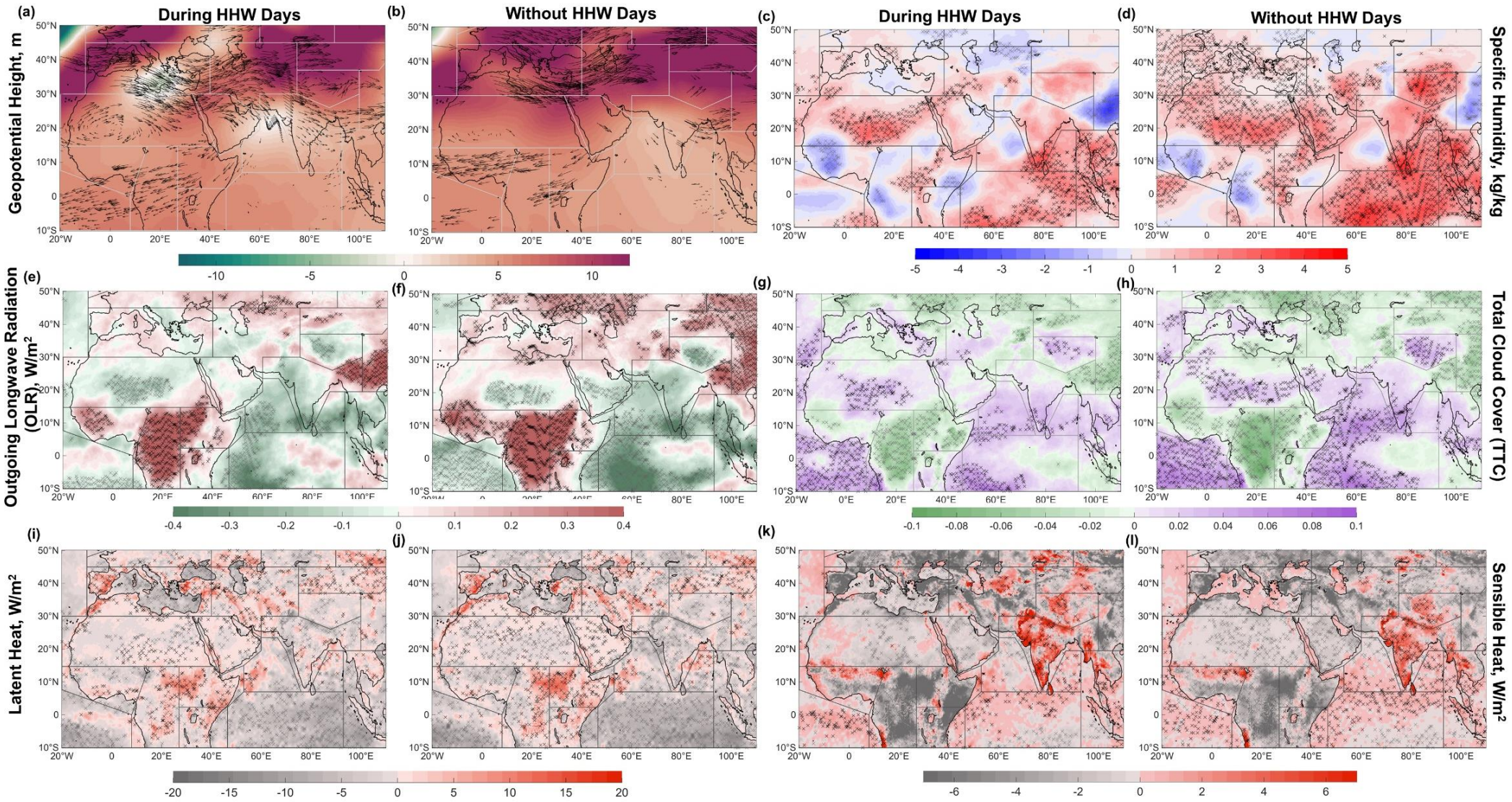

Figure 9: Difference in composite anomalies between the TW2 (2001–2024) and TW1 (1980–2000) for ET_x^w, shown for HHW vs. non-HHW days. Subplots show maps of TW2–TW1 differences in (a, b) **geopotential height** (m) at **500-hPa** with significant wind vectors overlaid. Wind with only significant ($p<0.10$) changes in average magnitude in 2001−2024 relative to baseline climatology 1991−2020 at each grid is shown using arrows. Statistical significance in mean wind magnitude changes is evaluated using the Wilcoxon rank-sum test at a 10% significance level. The arrow lengths indicate wind magnitude, while the arrowhead points to the direction from which the wind is blowing. The small arrow length in the wind vectors (*e.g.*, in Northwest Africa in fig. b) indicates the winds are relatively weak, while the large arrow length (e.g., in Northwest Africa in fig. b) indicates a region of strong winds. (c, d) **specific humidity at500-hPa** (kg kg^{-1}), (e–f) **outgoing longwave radiation (OLR)** (W m^{-2}), (g–h) **total cloud cover (TCC)** (fraction), (i–j) **latent heat flux (LHF)** (W m^{-2}), and (k–l) **sensible heat flux (SHF)** (W m^{-2}). Regions with statistically significant anomalies ($p < 0.01$) are denoted with stipples (black stipples: increase; grey stipples: decrease). All anomalies are computed relative to the baseline climatology (1991–2020).

1175

Supplementary information

for

Shifting Patterns of Summer Humid Heatwaves Highlight Growing Threat over South Asia and Middle East–North Africa

Saptashree Deb[1], Sparsha Rajesh Sherke[1], Poulomi Ganguli[1]

[1]Indian Institute of Technology Kharagpur, Kharagpur, India

Correspondence author's email: pganguli@agfe.iitkgp.ac.in

Contents of this file

Text S1

S1.1 Determination of Heatwave Magnitude using Accumulated Daily Heatwave Magnitude Index

We have determined the daily heatwave magnitude, M_{dly} (●) using the following equation (Russo et al. 2014; Lo et al. 2021):

$$M_{dly}\left(T_{dly}\right)=\begin{cases}\dfrac{T_{dly}-T_{25p}}{T_{75p}-T_{25p}}, \text{ if } T_{dly} > T_{25p}\end{cases} \quad (1)$$

Where T_{25p} and T_{75p} are the 25th and 75th percentile values of the daily maximum heat−humidity metrics series, T_{dly} considering the indices: Extended heat index (H_x) and wet-bulb temperature (T_x^w). A non-dimensional M_{dly} value of 3 indicates that the temperature anomaly on a day d with respect to T_{25p} is three times the interquartile range of T_{dly}, with the denominator of M_{dly} indicating a measure of the variability of annual T_{dly} time series. When a daily T_{dly} is less than the T_{25}, the M_{dly} value tends to be zero. In other words, the daily magnitude, M_{dly}, for any day during a heatwave with relatively milder temperatures are 0 and do not contribute to the heatwave intensity.

We identify extreme heatwave episodes (EH_x and ET_x^w) by implementing a daily variable temperature threshold to the T_{dly} time series (See Figure. 1b). We define an extreme HHW event when the daily maximum values of the at-site T_x^w (or H_x) value exceed the daily variable threshold of the 90th percentile and remain persistently above this threshold consecutively for more than three days or longer (Perkins and Alexander 2013; Perkins-Kirkpatrick and Gibson 2017) in both metrics. For e.g., ET_x^w for extreme HHW event detected from T_x^w, whereas EH_x are the events detected from H_x. For variable threshold determination, 366 (an additional day considering leap day of the year) heat-humidity metrics—duration (HHD) curves were drawn using the continuous T_{dly} series. Next, a centered moving mean window of 31 days (± 15-day) was employed as a smoothing filter to eliminate short-duration HHW events (Russo et al. 2014). We defined the extreme heat stress by accumulating the daily M_{dly} (●) values if they exceed the variable threshold consecutively for the time period of more than n days, where n = 3. We assess the severity of each event accumulated daily heatwave magnitude index (HWMId), which is the running sum of the daily heatwave magnitude over n (*i.e.,* $n \geq 3$) days comprising a single heatwave episode, which is expressed as below (Lo et al., 2021; Russo et al., 2014):

$$HWMId = \sum_{d=1}^{n} M_{dly}\left(T_{dly}\right) \quad (2)$$

S1.2 Jensen-Shannon (JS) divergence measures

The JS divergence measures the similarity between two probability distributions by averaging their Kullback-Leibler (KL) divergences relative to their midpoint distribution, providing a more reliable measure of their resemblance or dissimilarity. It is defined as below (Menéndez et al. 1997; Dhinakaran 2023):

$$JSD(P \parallel Q) = \frac{1}{2}D(P \parallel M) + \frac{1}{2}D(Q \parallel M) \quad (3)$$

where $M = \frac{1}{2}(P + Q)$ is a mixture distribution of P and Q and $D(P \parallel Q)$ is the Kullback-Leibler divergence. Here, P and Q represent the daily at-site T_{dly} distributions considering, T_x^w and H_x series in TW1 (1980−2000) and TW2 (2001−2024), respectively. The JSD value ranges between 0 (indicating identical distributions) and 1 (indicating maximum dissimilarity), providing insight into the degree of similarity or dissimilarity between two distributions. Since JSD varies from 0 to 1 and may not fully capture the regional magnitude of distributional shifts, we applied a spatial standardization by calculating the difference between at-site JSD and spatial mean JSD (derived from the mean of all at-site JSD values), divided by the corresponding spatial standard deviations of the JSDs (derived from the standard deviations of all at-site JSD values). At-site standardized JSD value indicates site-wise divergence to assess the relative shift in T_{dly} distribution from the normal condition for each region (Table S2).

S1.3 Analysing Trends in Consecutive Heatwave Events using Sen's Slope Estimator

We determine trends between two consecutive HHW events across each sites using a non-parametric slope estimator, Sen's slope method (Agarwal et al. 2021; Ray et al. 2021; Jiqin et al. 2023). As different sites belong to different climatological regions with varied ranges of temperature, to make trend estimates comparable across sites, we express the change statistics, T_S at location s in the units of percentage change per decade (i.e., 10 years) by normalizing the trend statistics S_s with mean of the series, $\bar{S}_s$ (Stahl et al. 2012; Gudmundsson et al. 2019)

$$T_S = \frac{S_s \times 100}{\bar{S}_s} \times 10 \tag{4}$$

Where, $S_s = \frac{X_j - X_i}{j - i}$ where, $s = 1,2....N$ and $j>I$

S_s in Eq. 4 indicates the Sen-Theil Slope estimator, X_j and X_i are the data points in time periods j and i $(j>i)$. To determine trend significance, following an earlier assessment (Gudmundsson et al. 2019), a non-parametric bootstrap resampling procedure is adopted considering $N = 1000$ bootstrap iterations. The trend significance is reported at a 10% significance levels, where $p < 0.10$ is considered for significant negative trends and $p > 0.90$ accounts for the significant positive trends (Gudmundsson et al. 2019).

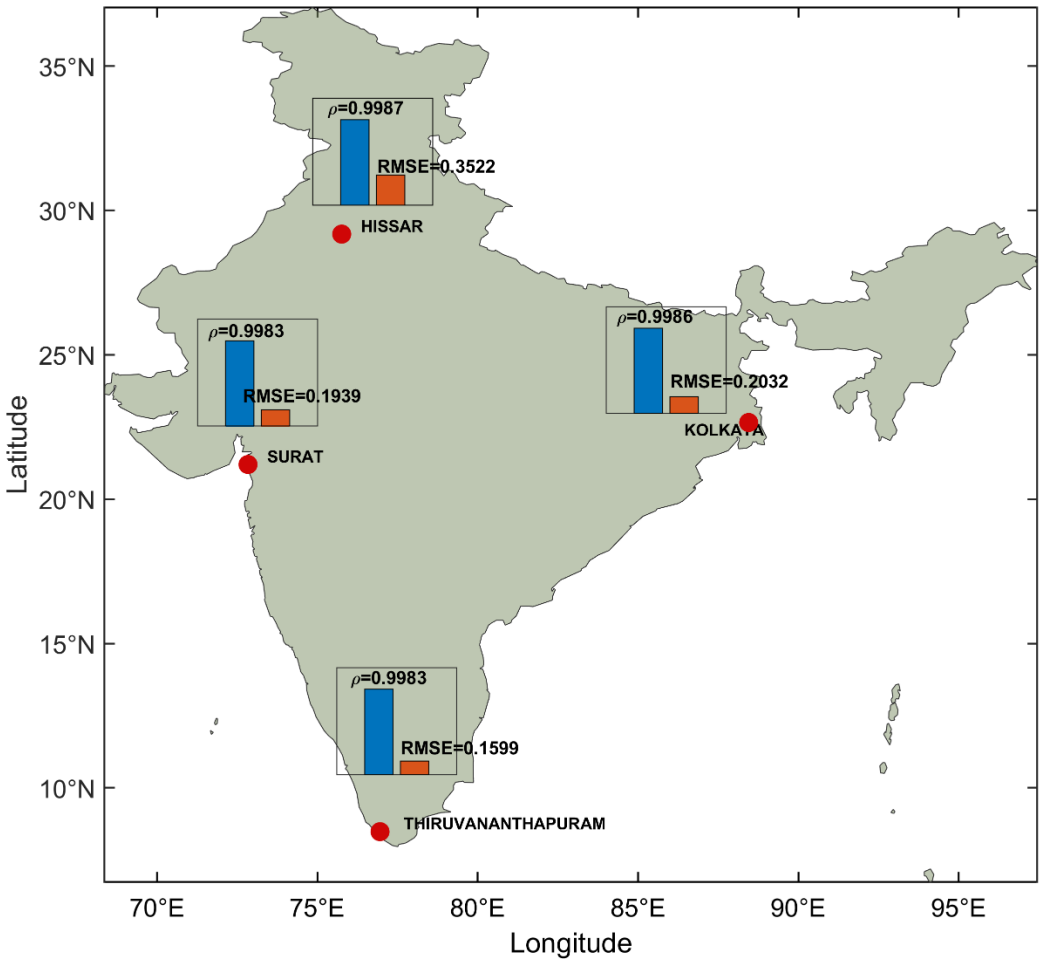

Figure S1. Validation of wet-bulb temperature (T_x^w) calculated using Davis-Jones method against the IMD-observed daily maxima wet-bulb temperature across four representative sites across Indian subcontinent for summer (Mar–Aug) during the period of 1980-2024. The map shows the locations of one station each from North (Hissar), West (Surat), East (Kolkata), and South (Thiruvananthapuram). At each site, inset bars summarize the agreement between the derived T_x^w and IMD-observed T_w for the hot-season (Mar–Aug), reporting Spearman's rank correlation (ρ) (using shaded bar in blue) and RMSE (using shaded bar in orange) (°C) computed from daily maximum T_x^w series. High ρ (≈0.99) and low RMSE (<0.36 °C) indicate strong consistency between the derived and the IMD-observed wet-bulb temperature across diverse climate settings within the Indian Subcontinent.

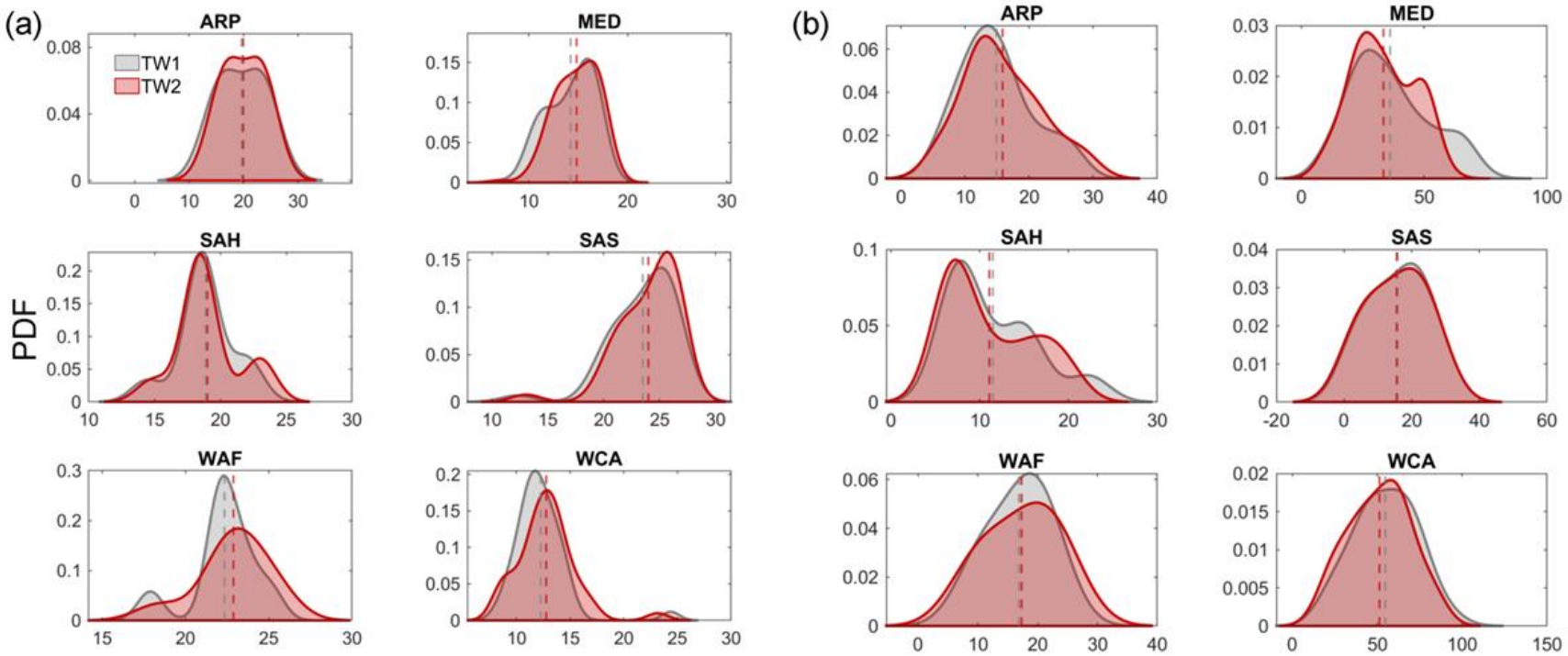

Figure S2: Probability density functions (PDFs) comparing (a) mean (°C) and (b) variance (°C^2) considering daily T_x^w, over two non-overlapping time windows: 2001-2024 vs 1980-2000, across the eight IPCC climate reference regions. The PDFs are obtained using the Kernel Density function. Dashed vertical lines represent the respective means of each distribution for each region. The PDFs are shown for regions with station counts of at least ten and higher.

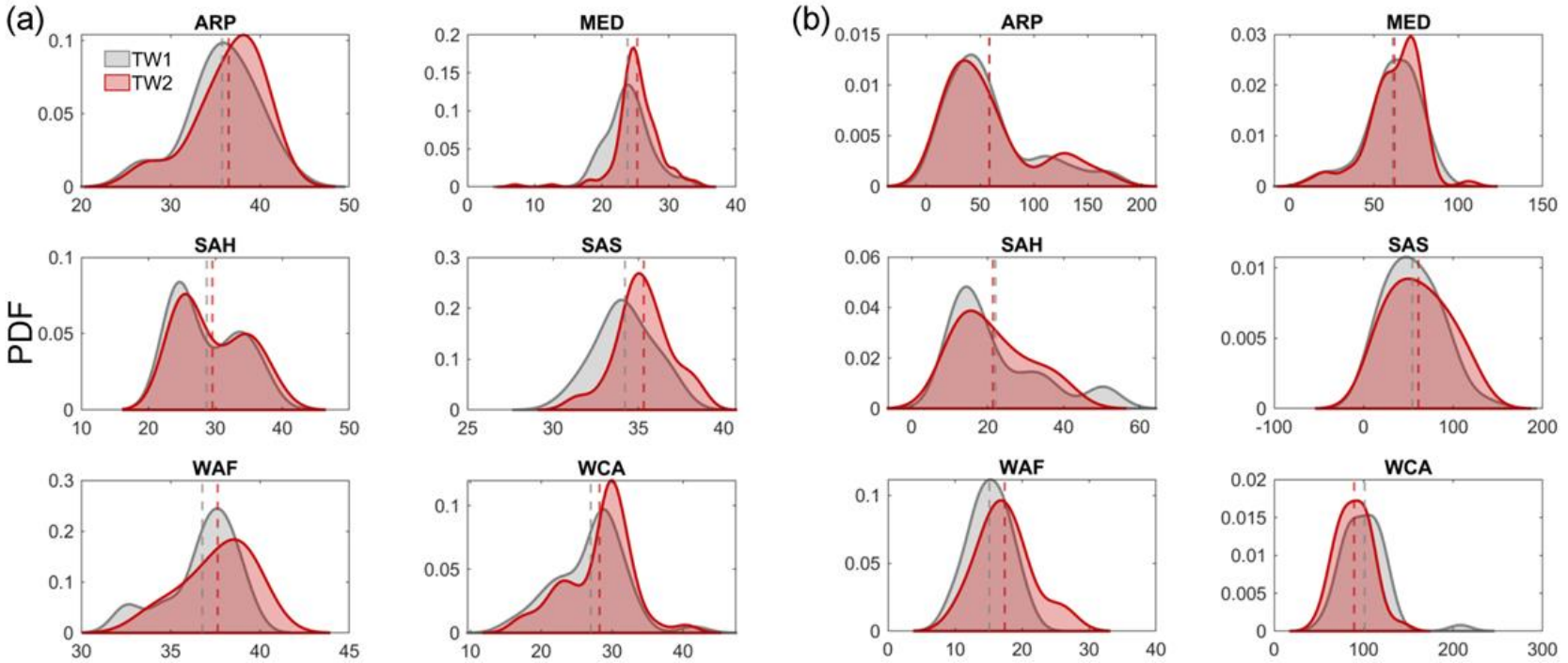

Figure S3: Probability density functions (PDFs) comparing (a) mean (°C) and (b) variance (°C^2) considering daily H_x, over two non-overlapping time windows: 2001-2024 vs 1980-2000, across the eight IPCC climate reference regions. The PDFs are obtained using Kernel Density function. Dashed vertical lines represent the respective means of each distribution. The PDFs are shown for regions with station counts of at least ten and higher.

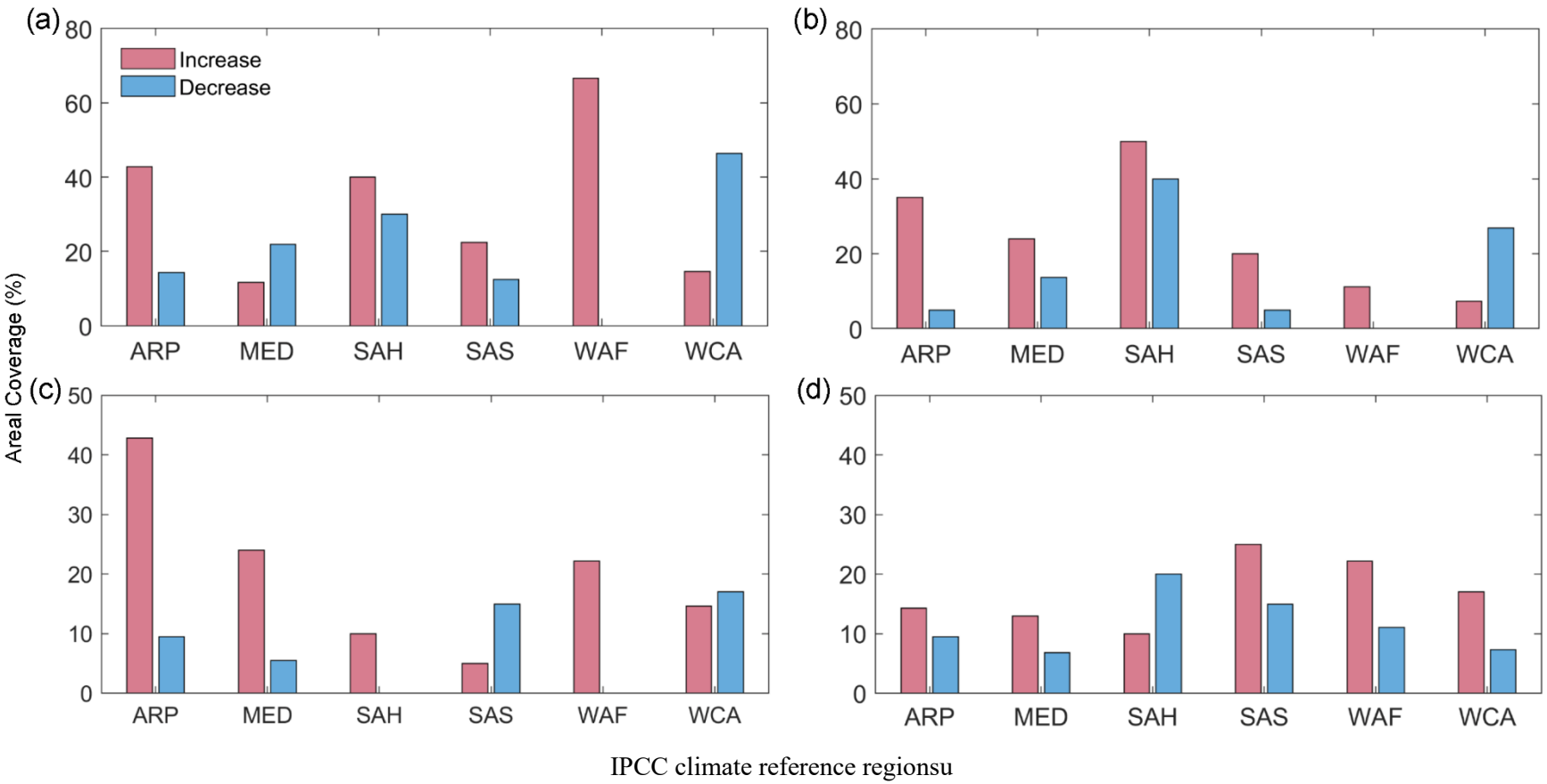

Figure S4: Histogram comparing the percentage share of stations with a significant ($p < 0.10$) increase (decrease) shifts in (a) mean and (b) variance for ET_x^w across the selected IPCC climate reference regions. (c - d) Same as in (a-b), but for EH_x. The histograms are shown for regions with station counts at least ten and higher.

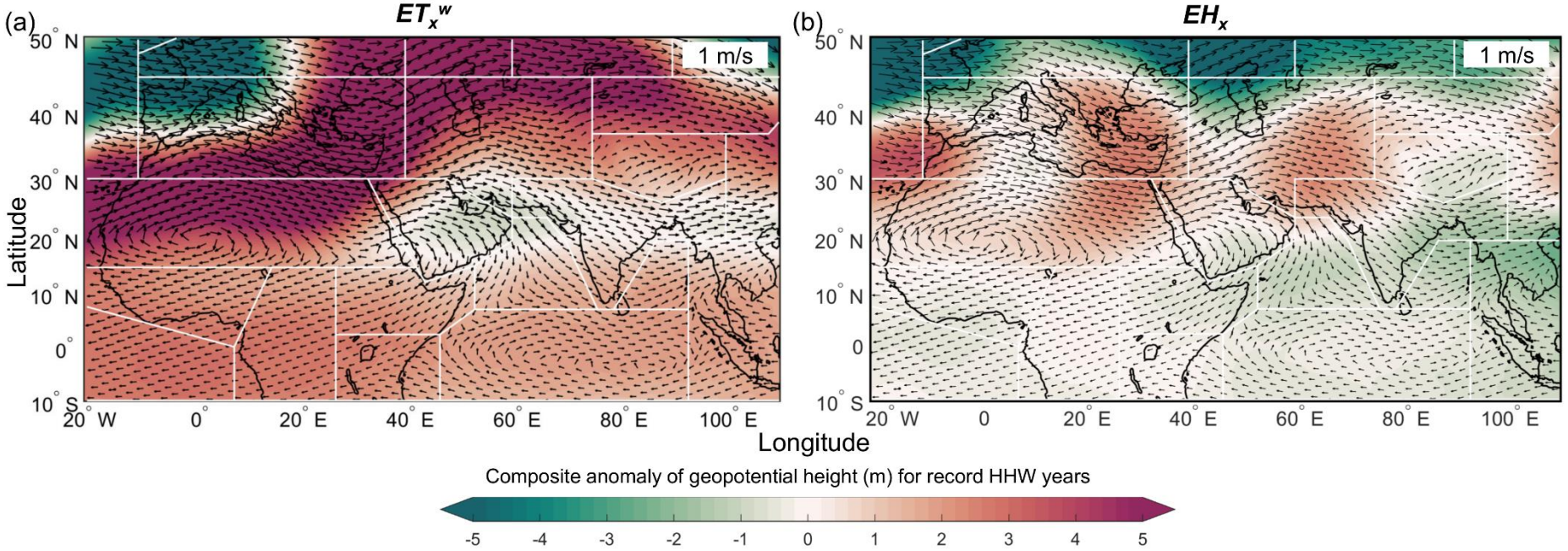

Figure S5. Composite anomaly plots of Geopotential height (500 hPa) superimposed with mean resultant wind vectors of the ten top hot years with the peak Accumulated daily Humid Heat Magnitude (HWMId) during the 40-year (1980−2024) analysis period for **(a)** ET_x^w and **(b)** EH_x. The arrow lengths in subplots **(a−b)** indicates wind magnitude, while the arrowhead points to the direction to which the wind is blowing. The small arrow length in the wind vectors indicates the winds are relatively weak, while large arrow length indicates region of strong winds.

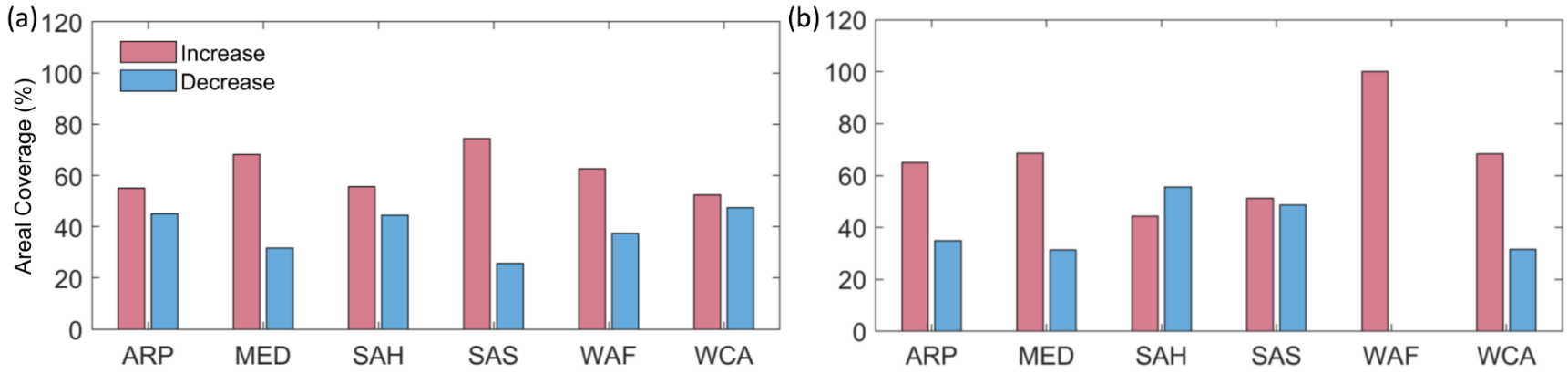

Figure S6: Histogram comparing the percentage share of stations with a significant ($p < 0.10$) increase (decrease) shifts in skewness considering (a) ET_x^w and (b) EH_x across the selected IPCC reference climate regions. The histograms are shown for regions with station counts at least ten and higher.

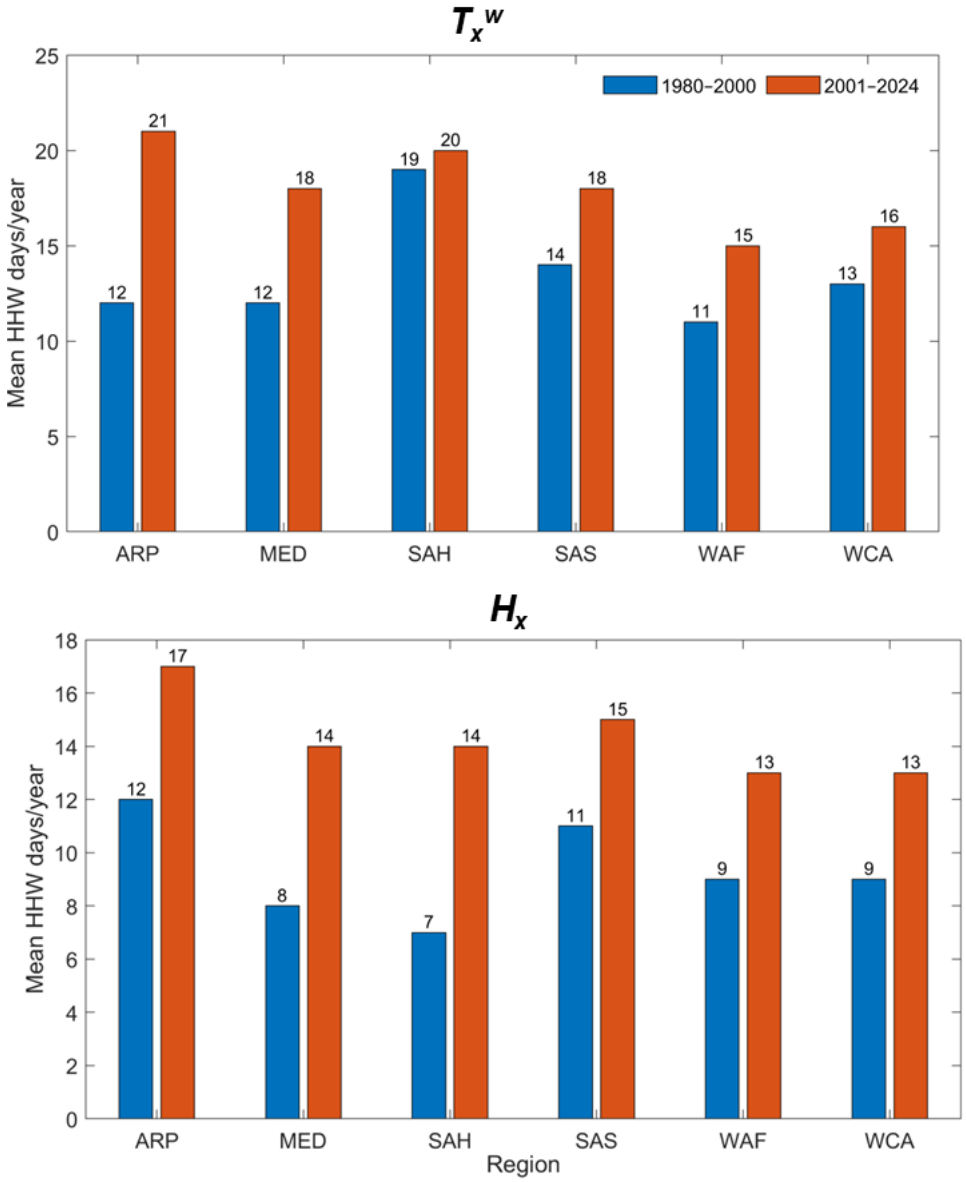

Figure S7. Histogram comparing the mean number of HHW days experienced/year for each region across the two non-overlapping time windows. Mean HHW days/year is determined based on (a) T_x^w and (b) H_x across the selected IPCC reference climate regions. Histograms are shown for regions with at least ten stations and higher counts.

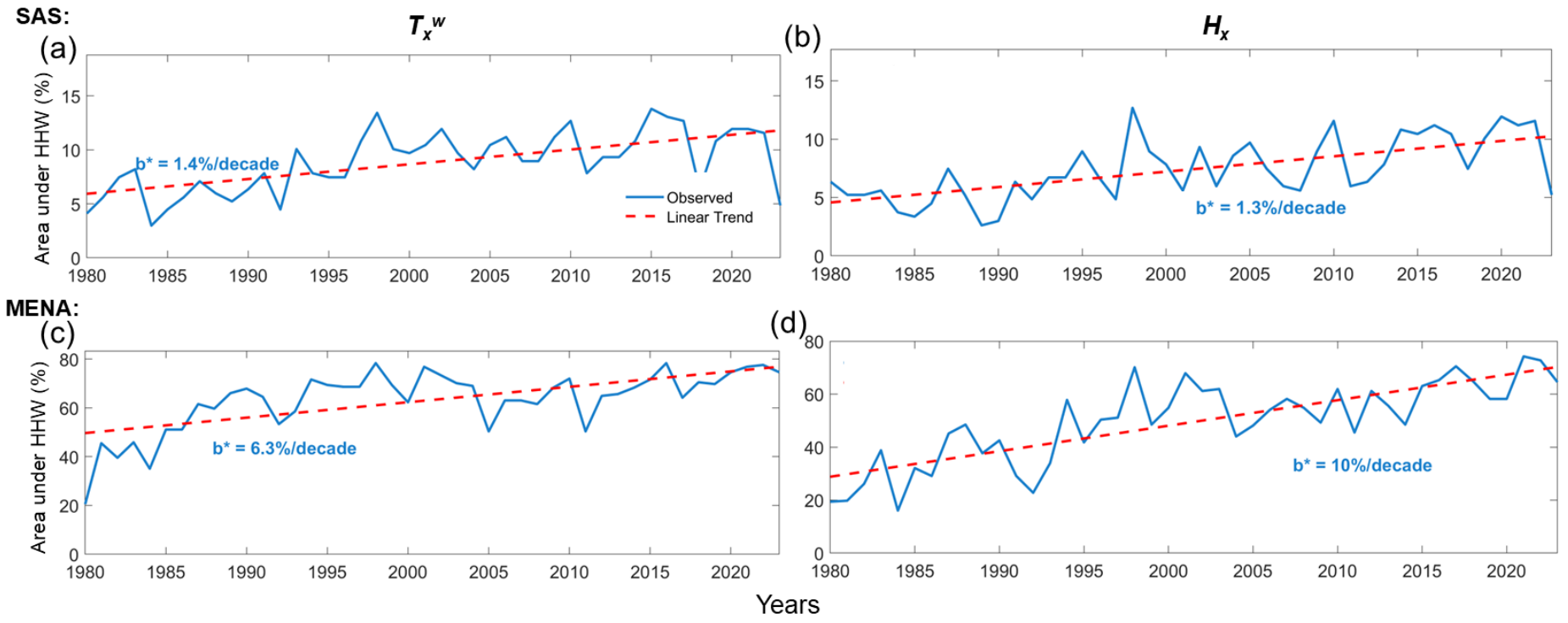

Figure S8: Areal coverage of HHWs across SAS and MENA during 1980–2024. Area affected by HHWs (in %) considering (a and c) ET_x^w and (b and d) EH_x. The solid blue curves show the observed annual areal coverage (in %), while the red dashed curves denote the least-squares linear regression fit, showing the trend in aerial coverage. Trend significance is assessed using an F-test; b* indicates statistically significant slopes ($P < 0.10$).

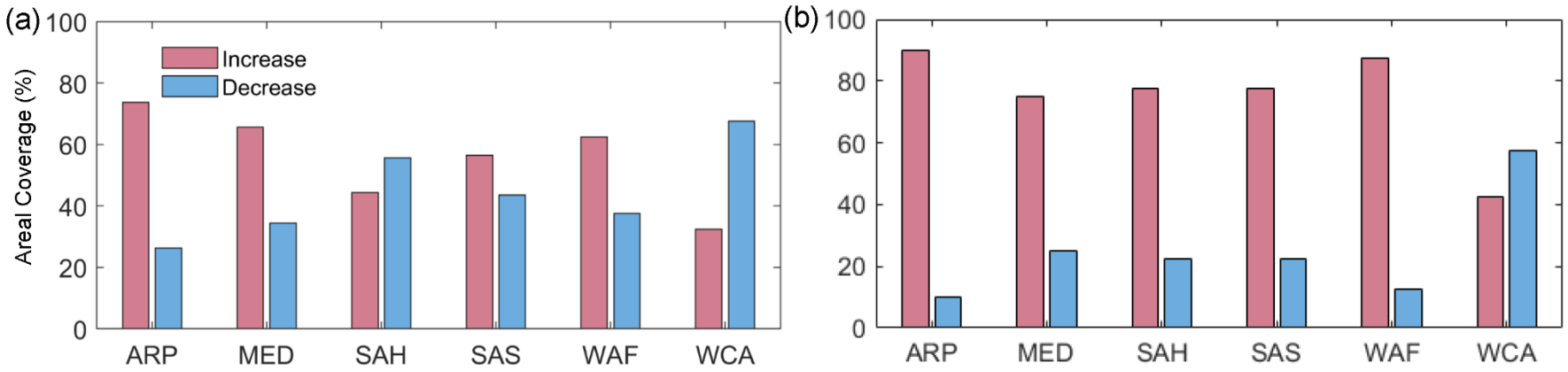

Figure S9: Histogram comparing the percentage share of stations with a significant ($p < 0.10$) increase (decrease) shifts in lag-1 autocorrelation for (a) ET_x^w and (b) EH_x across the selected IPCC reference climate regions. The histograms are shown for regions with station counts at least ten and higher.

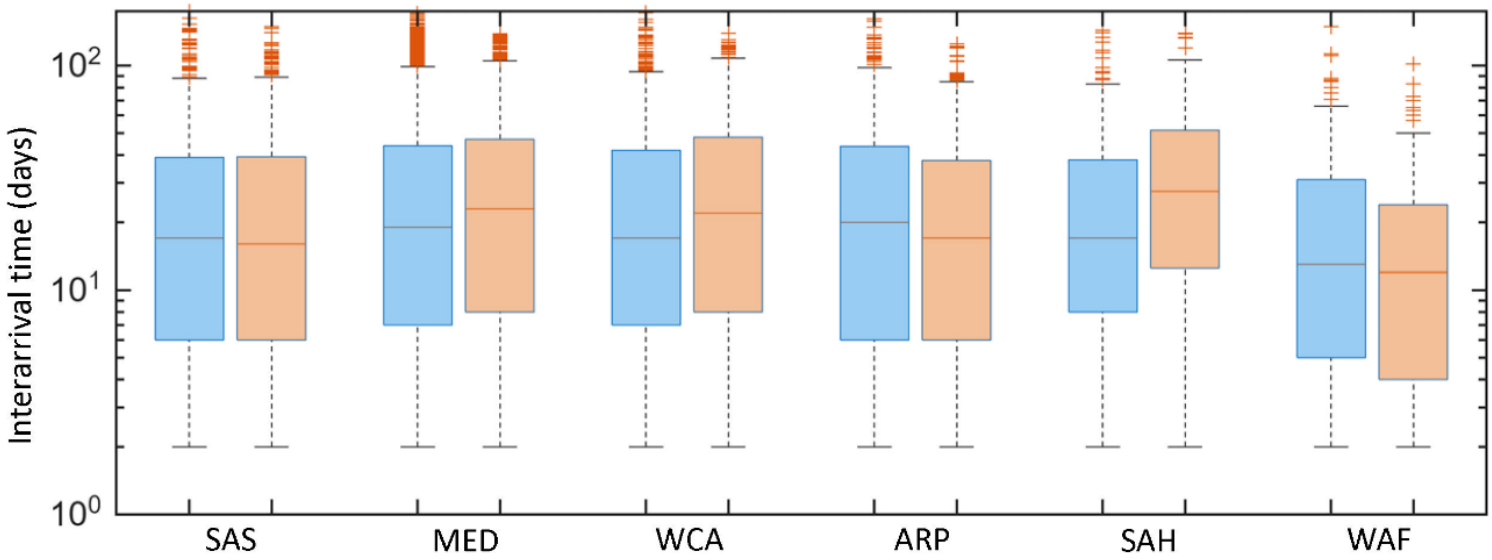

Figure S10: Regional variations in the inter-arrival times (days) comparing the two heat–humidity metrics. The spatial variations in interarrival times (days) across the selected IPCC reference climate regions (stations with at least ten and higher counts of stations) are shown using the boxplots. Box center marks (red lines) are medians; box bottom and top edges show 25th and 75th percentiles respectively, whereas the spread of the boxes indicates interquartile range; the top and bottom whiskers whiskers indicate $q_{75} + 1.5(q_{75} - q_{25})$ and $q_{25} - 1.5(q_{75} - q_{25})$, where q is the quantiles of variables. The outliers are indicated by orange '+' sign. The inter-arrival times considering two heat-humidity metrics, T_x^w and H_x are shown using shades of blue and orange, respectively.

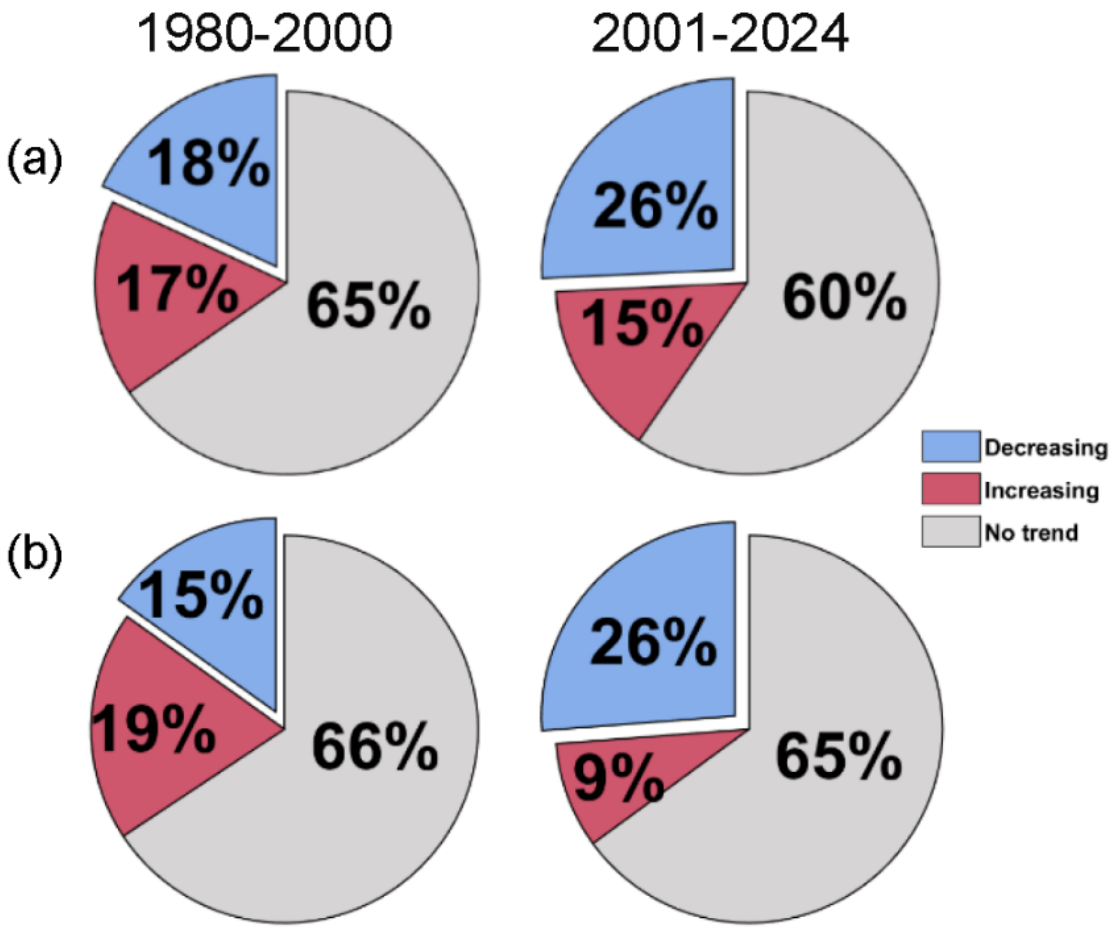

Figure S11: Pie charts comparing the fraction of sites with significant (increasing/decreasing) trends in inter-arrival time of HHW events considering **(a)** ET_x^w and **(b)** EH_x over two non-overlapping time windows, 2001-2024 vs. 1980-2000.

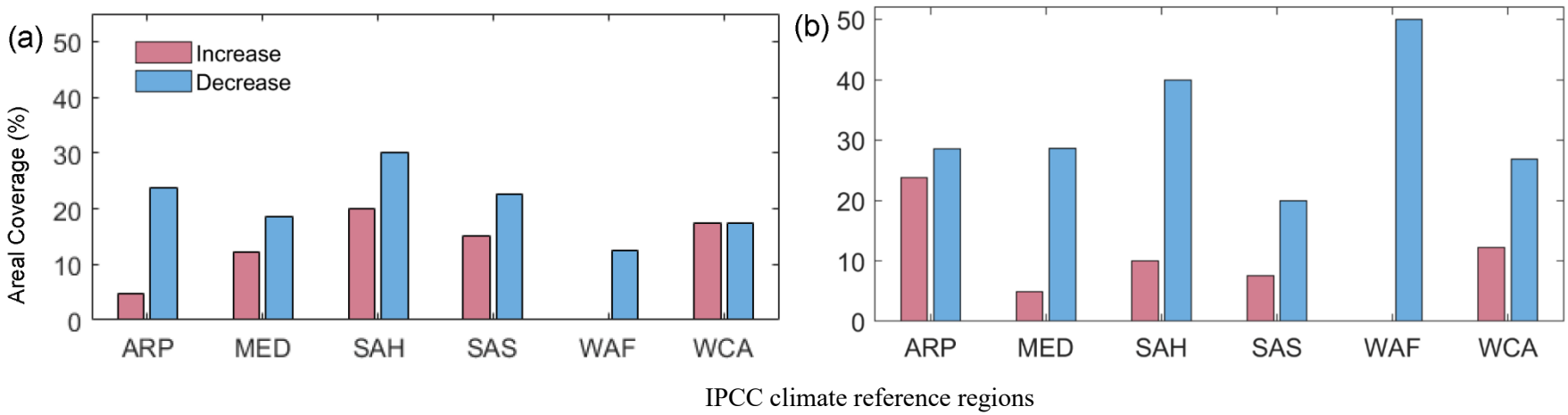

Figure S12: Histogram comparing the percentage share of stations with a significant ($p < 0.10$) increase (decrease) shifts in interarrival times considering (a) ET_x^w and (b) EH_x across selected climate reference regions. The histograms are shown for regions with station counts at least ten and higher.

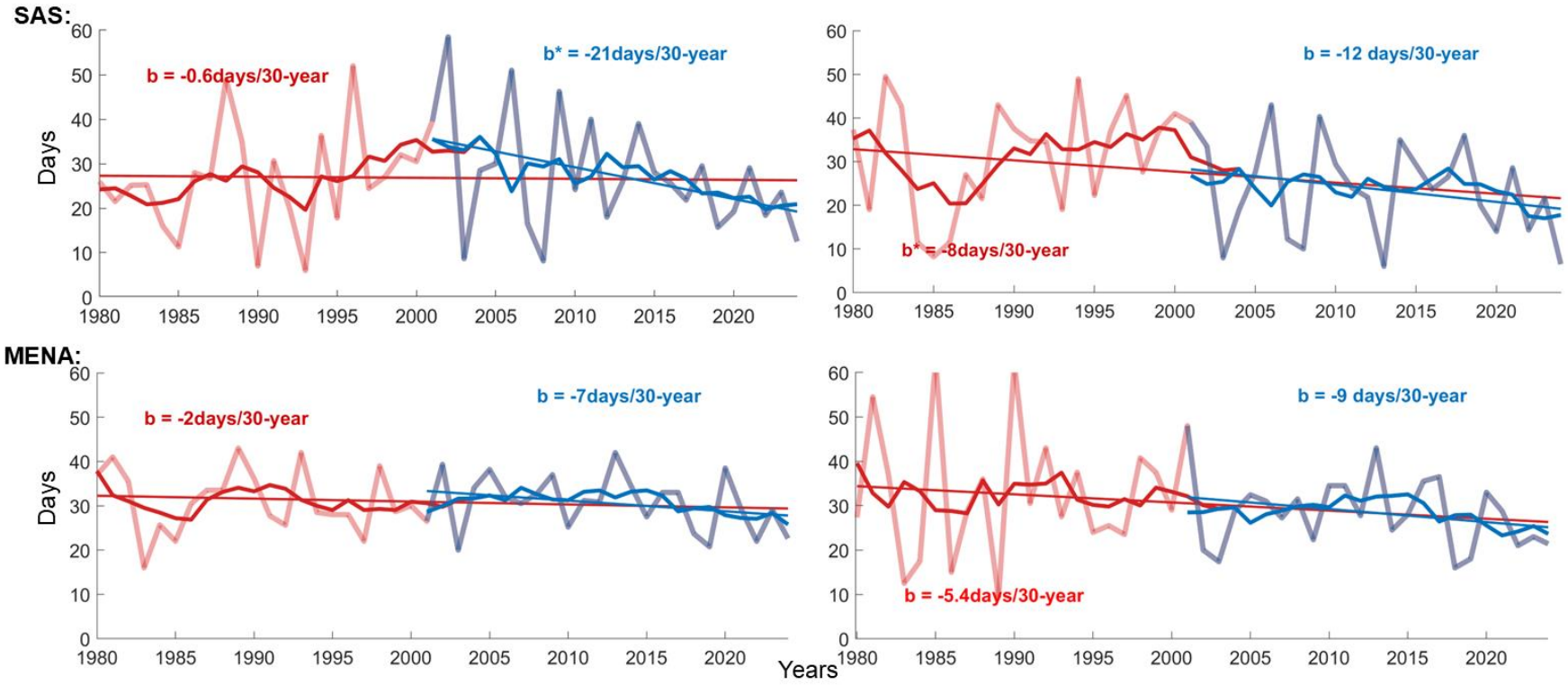

Figure S13: Trends in inter-arrival time of HHWs over SAS and MENA during 1980–2024. Year-wise mean inter-arrival times (days) considering (a and c) ET_x^w and (b and d) EH_x. The annual mean series (days) are smoothed using a 7-year moving average (solid curves). while the red dashed curves denote the least-squares linear regression fit, showing the trend in the interarrival time (days/30-year). Trend significance is assessed using an F-test; b* indicates statistically significant slopes ($p < 0.10$).

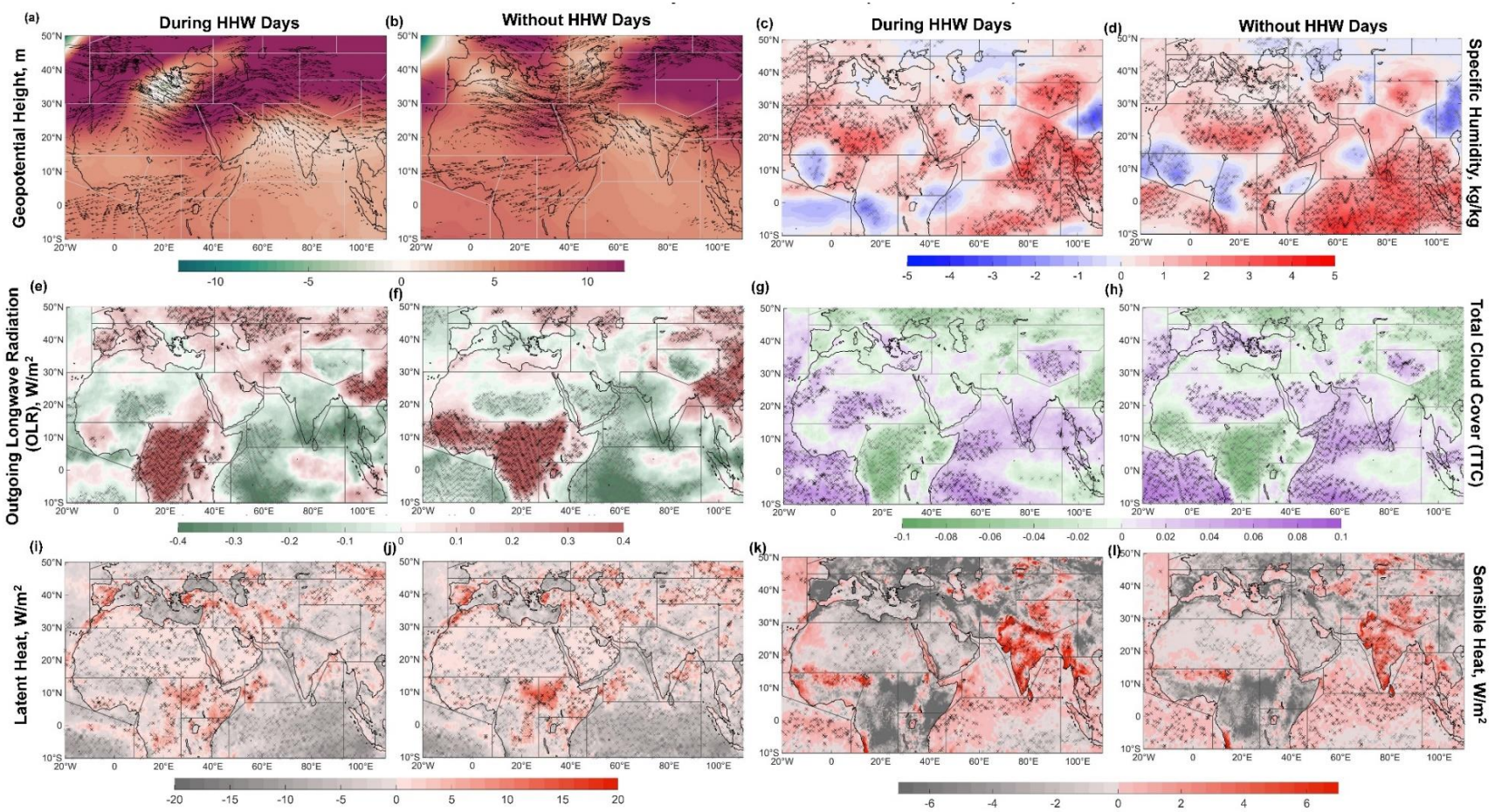

Figure S14: Difference in composite anomalies between the TW2 (2001–2024) and TW1 (1980–2000) for EH_x, shown for HHW vs. non-HHW days. Subplots show maps of TW2–TW1 differences in (a, b) geopotential height (m) at 500-hPa with significant wind vectors overlaid. Wind with only significant ($p<0.10$) changes in average magnitude in 2001−2024 relative to baseline climatology 1991−2020 at each grid is shown using arrows. Statistical significance in mean wind magnitude changes is evaluated using the Wilcoxon rank-sum test at a 10% significance level. The arrow lengths indicate wind magnitude, while the arrowhead points to the direction from which the wind is blowing. The small arrow length in the wind vectors (*e.g.,* in Northwest Africa in fig. b) indicates the winds are relatively weak, while the large arrow length (e.g., in Northwest Africa in fig. b) indicates a region of strong winds. (c, d) specific humidity at 500-hPa (kg kg^{-1}), (e–f) outgoing longwave radiation (OLR) (W m^{-2}), (g–h) total cloud cover (TCC) (fraction), (i–j) latent heat flux (LHF) (W m^{-2}), and (k–l) sensible heat flux (SHF) (W m^{-2}). Regions with statistically significant anomalies ($p < 0.01$) are denoted with stipples (black stipples: increase; grey stipples: decrease). All anomalies are computed relative to the baseline climatology (1991–2020).

Table S1: Cities selected over SAS and MENA

Sl. No.	HadISD_ID1	Lat	Long	Elevation (m)	Cities
1	132690	44.317	19.917	177	VALJEVO
2	132720	44.818	20.309	102.1	BEOGRAD
3	132740	44.8	20.467	132	BEOGRAD
4	132790	44.367	20.95	122	SMEDEREVSKA PALANKA
5	132850	44.75	21.517	84	VELIKO GRADISTE
6	133830	43.567	21.35	167	KRUSEVAC
7	133840	43.933	21.383	125	CUPRIJA
8	133970	43.017	22.75	450	DIMITROVGRAD
9	134570	42.405	18.723	6.1	TIVAT
10	135860	41.962	21.621	238	SKOPJE
11	143140	44.533	14.483	53	MALI LOSINJ
12	143230	45	14.9	28	SENJ
13	143280	45.267	15.233	328	OGULIN
14	143300	44.55	15.367	565	GOSPIC
15	144380	43.733	15.917	75	SIBENIK
16	144470	43.167	16.45	25	HVAR
17	146540	43.867	18.433	638	SARAJEVO-BJELAVE
18	153500	45.15	26.817	97	BUZAU
19	153600	45.167	29.733	9	SULINA
20	153660	44.883	22.417	176	BAILE HERCULANE
21	153690	44.883	23.7	265	TARGU LOGRESTI
22	153730	44.85	24.817	315	PITESTI
23	153750	44.933	25.433	297.7	TARGOVISTE
24	153870	44.9	29.6	2	SFANTU GHEORGHE DELTA
25	153950	44.667	24.233	281	DRAGASANI
26	154060	44.683	27.95	38	HARSOVA
27	154090	44.767	28.883	38	JURILOVCA
28	154100	44.633	22.633	80	DROBETA TURNU SEVERIN
29	154120	44.483	23.117	313	BACLES
30	154160	44.567	24.8	210	STOLNICI
31	154200	44.503	26.102	90.5	AUREL VLAICU
32	154250	44.55	27.4	52	SLOBOZIA
33	154340	44.433	24.35	173	SLATINA
34	154440	44.367	27.85	61	FETESTI
35	154620	44.25	28.267	72	MEDGIDIA
36	154690	44.1	24.367	107	CARACAL
37	154820	43.983	22.95	63	CALAFAT
38	154890	43.983	25.35	76	ALEXANDRIA
39	154910	43.883	25.95	24	GIURGIU
40	154980	43.667	25.35	34	ZIMNICEA
41	156550	42.57	27.515	41.1	BURGAS
42	161200	44.412	8.842	4	GENOVA SESTRI
43	161400	44.535	11.289	37.5	BOLOGNA
44	161490	44.02	12.612	12.5	RIMINI

45	161530	43.95	8.167	221	CAPE MELE
46	161580	43.684	10.393	1.8	PISA
47	161700	43.81	11.205	43.9	FIRENZE
48	162300	42.432	14.181	14.6	PESCARA
49	162420	41.804	12.251	4.6	FIUMICINO
50	162610	41.541	15.718	55.8	AMENDOLA
51	162700	41.133	16.767	53.9	BARI
52	162800	40.917	12.95	185	PONZA ISLAND
53	163100	40.017	15.283	185	CAPE PALINURO
54	163200	40.658	17.947	14.3	CASALE
55	163250	40.433	16.883	12	MARINA DI GINOSA
56	163600	39.817	18.35	112	SANTA MARIA DI LEUC
57	164000	38.7	13.183	251	USTICA ISLAND
58	164050	38.176	13.091	19.8	PALERMO
59	164200	38.2	15.55	51	MESSINA
60	164290	37.911	12.488	7.3	TRAPANI BIRGI
61	164530	37.083	14.217	33	GELA
62	164600	37.467	15.066	11.9	CATANIA FONTANAROSSA
63	164800	36.683	15.133	51	COZZO SPADARO
64	165200	40.632	8.291	26.5	ALGHERO
65	165600	39.251	9.054	4	ELMAS
66	165970	35.857	14.478	91.4	LUQA
67	166140	40.446	21.282	660.5	ARISTOTELIS
68	166220	40.52	22.971	6.7	MAKEDONIA
69	166270	40.856	25.956	7.3	DIMOKRITOS
70	166410	39.602	19.912	1.8	IOANNIS KAPODISTRIAS INTL
71	166430	38.925	20.765	3.4	AKTIO
72	166480	39.65	22.466	73.5	LARISA
73	166500	39.917	25.236	4.3	LIMNOS
74	166670	39.057	26.598	18.3	MITILINI
75	166820	37.921	21.293	16.8	ANDRAVIDA
76	166840	38.968	24.487	13.4	SKIROS
77	167100	37.531	22.404	644	TRIPOLIS
78	167160	37.882	23.735	21	ATHINAI
79	167320	37.1	25.367	9.8	NAXOS
80	167460	35.532	24.15	149.4	SOUDA
81	167464	35.533	24.15	146.3	SOUDA BAY CRETE
82	167490	36.405	28.086	5.8	DIAGORAS
83	170240	41.983	33.783	64	INEBOLU
84	170260	42.033	35.167	32	SINOP
85	170560	40.983	27.55	3	TEKIRDAG
86	170600	40.977	28.821	49.7	ATATURK
87	170700	40.733	31.6	743	BOLU
88	170840	40.55	34.95	776	CORUM
89	171120	40.138	26.427	7	CANAKKALE
90	171160	40.183	29.067	100	BURSA
91	171240	39.784	30.582	786.7	ESKISEHIR
92	171280	40.128	32.995	952.5	ESENBOGA

93	171500	39.619	27.926	103.6	BALIKESIR
94	171840	38.809	27.834	80.2	AKHISAR
95	171880	38.681	29.472	883	USAK
96	172190	38.292	27.157	125.6	ADNAN MENDERES
97	172600	36.947	37.479	705.6	OGUZELI
98	172800	37.894	40.201	686.1	DIYARBAKIR
99	172900	37.14	27.67	61.6	IMSIK
100	172920	37.217	28.367	646	MUGLA
101	173000	36.899	30.8	53.9	ANTALYA
102	173300	36.383	33.933	15	SILIFKE
103	173500	37.002	35.426	72.5	INCIRLIK AB
104	173700	36.573	36.154	7.6	ISKENDERUN
105	176000	34.718	32.486	12.5	PAFOS INTL
106	176010	34.59	32.988	23.2	AKROTIRI
107	176090	34.875	33.625	2.4	LARNACA
108	370310	44.983	41.117	159	ARMAVIR
109	370540	44.225	43.082	321.3	MINERALNYYE VODY
110	370610	44.783	44.133	136	BUDENNOVSK
111	372280	43.033	44.683	703	VLADIKAVKAZ
112	374720	43	47.5	-18.6	MAHACHKALA
113	375490	41.75	44.767	427	TBILISI
114	379850	38.733	48.833	-12	LANKARAN
115	380010	43.86	51.092	22.3	AKTAU
116	380620	44.706	65.591	132	KZYL-ORDA
117	381780	43.15	64.333	234	AK-BAJTAL
118	381980	43.267	68.217	207	TURKESTAN
119	382320	42.967	54.117	78	AKKUDUK
120	382620	42.95	59.817	66	CHIMBAJ
121	383410	42.85	71.3	652	TARAZ
122	383880	41.033	57.767	62	EKEZHE
123	383920	41.75	59.817	82	DASHKHOVUZ
124	383960	41.567	60.633	101	URGENCH
125	384030	41.75	62.467	98	BUZAUBAJ
126	384130	41.733	64.617	238	TAMDY-BULAK
127	384390	41.367	68	275	SHARDARA
128	384570	41.258	69.281	431.9	YUZHNY
129	385450	40.467	62.283	142	DARGANATA
130	386180	40.367	71.75	603.5	FERGANA AIRPORT
131	386870	39.083	63.6	190	CHARDZHEV
132	386960	39.701	66.984	677.9	SAMARKAND
133	387500	37.467	53.967	-22	ESENGULY
134	387630	38.983	56.283	92	GYZYLARBAT
135	388800	37.987	58.361	210.9	ASHGABAT
136	388950	37.6	62.183	240	BAJRAMALY
137	389110	37.822	65.135	243.2	KERKI INTL
138	389270	37.287	67.31	313	TERMEZ
139	389870	35.283	62.35	625	GYSHGY
140	400800	33.412	36.516	615.7	DAMASCUS INTL

141	400950	32.6	36.1	543	DARA A
142	401990	29.561	34.96	12.8	EILAT
143	402700	31.973	35.992	778.8	MARKA INTL
144	403570	30.907	41.138	552.6	ARAR
145	403600	31.412	37.279	509.6	GURIAT
146	403610	29.785	40.1	689.2	AL JOUF
147	403730	28.335	46.125	357.8	QAISUMAH
148	403750	28.365	36.619	777.5	TABUK
149	404000	26.199	36.476	20.1	WEJH
150	404050	26.3	43.767	648	GASSIM
151	404160	26.265	50.152	25.6	KING ABDULAZIZ AB
152	404300	24.553	39.705	655.6	PRINCE MOHAMMAD BIN ABDULAZIZ
153	404370	24.958	46.699	624.5	KING KHALED INTL
154	404380	24.722	46.725	635.2	KING SALMAN AB
155	404390	24.144	38.063	7.9	YENBO
156	405820	29.227	47.969	62.8	KUWAIT INTL
157	407040	38.433	47.067	1390	AHAR
158	407060	38.134	46.235	1359.1	TABRIZ
159	407450	36.235	59.641	994.6	MASHHAD
160	407630	35.2	58.467	1109	KASHMAR
161	408530	29.233	56.567	2280	BAFT
162	408780	27.333	62.333	1195	SARAVAN
163	410240	21.68	39.157	14.6	KING ABDULAZIZ INTL
164	411360	17.467	47.121	720.2	SHARURAH
165	411700	25.261	51.565	10.7	DOHA
166	412400	26.217	56.25	4	KHASAB PORT
167	412560	23.593	58.284	14.6	SEEB INTL
168	412680	22.533	59.483	14	SUR
169	413160	17.039	54.091	22.3	SALALAH
170	417800	24.907	67.161	30.5	JINNAH INTL
171	421310	29.179	75.755	213.4	HISSAR
172	421820	28.585	77.206	214.9	SAFDARJUNG
173	423280	26.9	70.917	231	JAISALMER
174	423390	26.251	73.049	218.5	JODHPUR
175	423690	26.761	80.889	125	LUCKNOW
176	423790	26.74	83.45	78.9	GORAKHPUR
177	424100	26.106	91.586	49.4	GUWAHATI INTL
178	424520	25.16	75.846	273.1	KOTA
179	425030	25.02	88.08	26	MALDAH
180	425710	24.567	80.833	317	SATNA
181	425910	24.744	84.951	115.8	GAYA
182	426470	23.077	72.635	57.6	AHMEDABAD
183	427060	23.14	87.04	78	BANKURA
184	427080	23.39	87.42	49	SRINIKETAN
185	427240	23.887	91.24	14	AGARTALA
186	427370	22.309	70.78	134.4	RAJKOT
187	427980	22.813	86.169	153.9	JAMSHEDPUR

188	428070	22.53	88.33	9	KOLKATA (CALCUTTA)
189	428090	22.655	88.447	4.9	KOLKATA NETAJI SUBHASH CHANDRA BOSE INT AIRPORT
190	428400	21.2	72.833	12	SURAT
191	428670	21.1	79.05	309	NAGPUR
192	429010	21.63947	87.50811	4	DIGHA
193	429700	20.4625	85.88	34	CUTTACK
194	429710	20.244	85.818	42.1	BHUBANESHWAR
195	429760	20.18	86.41	1	PARADEEP
196	430490	19.16	84.53	11	GOPALPUR
197	430530	19.8135	85.8312	24	PURI
198	430570	19.26464	73.04367	18	MUMBAI/COLABA
199	430630	18.53	73.85	560	PUNE
200	431170	17.628	75.935	482.8	SHOLAPUR
201	431280	17.27	78.28	13	HYDERABAD
202	431490	17.6868	83.2185	10	VISAKHAPATNAM
203	432840	12.961	74.89	102.7	MANGALORE
204	433140	11.25	75.783	5	KOZHIKODE
205	433290	11.46	79.46	11	CUDDALORE
206	433440	10.765	78.71	87.8	TIRUCHIRAPPALLI
207	433520	9.4981	76.3388	21	ALAPUZAH
208	433710	8.483	76.95	64	THIRUVANANTHAPURAM
209	600200	28.45	-16.25	36	STA. CRUZ DE TENERIFE
210	600250	28.044	-16.572	63.7	TENERIFE SUR
211	600300	27.932	-15.387	23.8	GRAN CANARIA
212	600350	28.453	-13.864	25.3	FUERTEVENTURA
213	600400	28.945	-13.605	14.3	LANZAROTE
214	601010	35.727	-5.917	18.9	IBN BATOUTA
215	601070	35.177	-3.84	27.1	CHERIF EL IDRISSI
216	601150	34.787	-1.924	467.9	ANGADS
217	601410	33.927	-4.978	579.1	SAISS
218	601500	33.879	-5.515	576.1	BASSATINE
219	601560	33.367	-7.59	199.9	MOHAMMED V
220	602300	31.607	-8.036	467.9	MENARA
221	602520	30.325	-9.413	76.2	AL MASSIRA
222	603180	35.594	-5.32	3	SANIAT RMEL
223	603380	35.28	-2.956	47.5	MELILLA
224	603510	36.795	5.874	11	FERHAT ABBAS AIRPORT
225	603600	36.822	7.809	4.9	ANNABA
226	603900	36.691	3.215	25	HOUARI BOUMEDIENE
227	604020	36.712	5.07	6.1	SOUMMAM
228	604900	35.624	-0.621	89.9	ES SENIA
229	605310	35.017	-1.45	248.1	ZENATA
230	605550	33.068	6.089	85	SIDI MAHDI
231	605660	32.384	3.794	460.9	NOUMERAT
232	605900	30.571	2.86	398.1	EL GOLEA
233	606110	28.052	9.643	563	IN AMENAS
234	607100	36.98	8.877	70.1	TABARKA 7 NOVEMBRE

235	607150	36.851	10.227	6.7	CARTHAGE
236	607200	36.85	11.083	30	KELIBIA
237	607350	35.667	10.1	68	KAIROUAN
238	607400	35.667	10.75	2	MONASTIR-SKANES
239	607450	34.422	8.823	323.1	GAFSA
240	607500	34.718	10.691	25.9	THYNA
241	607600	33.94	8.111	87.5	NEFTA
242	607690	33.875	10.775	5.8	ZARZIS
243	610520	13.482	2.184	223.1	DIORI HAMANI
244	610750	13.8	5.25	273	BIRNI-N KONNI
245	610900	13.779	8.984	462.1	ZINDER
246	616000	16.051	-16.463	2.7	SAINT LOUIS
247	616410	14.74	-17.49	25.9	LEOPOLD SEDAR SENGHOR INTL
248	616790	14.147	-16.051	7.9	KAOLACK
249	616870	13.737	-13.653	49.1	TAMBACOUNDA
250	616950	12.556	-16.282	22.9	ZIGUINCHOR
251	617010	13.338	-16.65	29	BANJUL
252	619720	22.333	40.333	6	ILE EUROPA
253	619760	15.883	54.517	13	SERGE-FROLOW (ILE TROMELIN)
254	619900	20.43	57.684	56.7	SIR SEEWOOSAGUR RAMGOOLAM INT
255	623180	31.184	29.949	5	ALEXANDRIA
256	623660	30.122	31.406	116.4	CAIRO
257	624050	25.671	32.707	89.6	LUXOR INTL
258	627210	15.589	32.553	385.6	KHARTOUM
259	646500	4.398	18.519	368.2	BANGUI M POKO
260	647000	12.134	15.034	295	NDJAMENA
261	655020	13.567	-2.417	336	OUAHIGOUYA
262	655030	12.353	-1.512	316.1	OUAGADOUGOU
263	688160	33.965	18.602	46	CAPE TOWN INTL
264	688280	34.006	22.379	197.5	GEORGE
265	688420	33.985	25.617	68.9	PORT ELIZABETH INTL
266	688580	33.036	27.826	132.6	EAST LONDON
267	689060	40.35	-9.883	54	GOUGH ISLAND
268	689940	46.875	37.86	22	MARION ISLAND

Table S2: Standardized anomaly of JSD values over SAS and MENA regions with their interpretation

SA*	**Interpretation**
>-0.5 to < 0.5 including 0s and close to 0	Similar Distribution
>-1 to <-0.5 and > 0.5 to < 1	Nearly Similar Distribution
>-2 to <-1 and > 1 to < 2	Moderately Dissimilar Distribution
>-3 to <-2 and > 2 to < 3	Dissimilar Distribution
<-3 or > 3	Extremely Dissimilar Distribution

*The SA values are obtained using: $SA = \frac{X_i - \mu_{IPCC\ Region}}{\sigma_{IPCC\ Region}}$, Where, X_i is the at-site JSD values for H_x and T_x^w series, $\mu_{IPCC\ Region}$ is the mean and $\sigma_{IPCC\ Region}$ is the standard deviation of all the at-site X_i values of each IPCC reference climate regions.

References

Agarwal S, Suchithra AS, Gurjar SP (2021) Analysis and Interpretation of Rainfall Trend using Mann-Kendall's and Sen's Slope Method. Indian J Ecol 48:453–457

Dhinakaran A (2023) How to Understand and Use the Jensen-Shannon Divergence. In: Medium. https://medium.com/data-science/how-to-understand-and-use-jensen-shannon-divergence-b10e11b03fd6. Accessed 23 Jul 2025

Gudmundsson L, Leonard M, Do HX, et al (2019) Observed Trends in Global Indicators of Mean and Extreme Streamflow. Geophys Res Lett 46:756–766. https://doi.org/10.1029/2018GL079725

Jiqin H, Gelata FT, Chaka Gemeda S (2023) Application of MK trend and test of Sen's slope estimator to measure impact of climate change on the adoption of conservation agriculture in Ethiopia. J Water Clim Change 14:977–988. https://doi.org/10.2166/wcc.2023.508

Lo S-H, Chen C-T, Russo S, et al (2021) Tracking heatwave extremes from an event perspective. Weather Clim Extrem 34:100371. https://doi.org/10.1016/j.wace.2021.100371

Menéndez ML, Pardo JA, Pardo L, Pardo MC (1997) The Jensen-Shannon divergence. J Frankl Inst 334:307–318. https://doi.org/10.1016/S0016-0032(96)00063-4

Perkins SE, Alexander LV (2013) On the measurement of heat waves. J Clim 26:4500–4517. https://doi.org/10.1175/JCLI-D-12-00383.1

Perkins-Kirkpatrick SE, Gibson PB (2017) Changes in regional heatwave characteristics as a function of increasing global temperature. Sci Rep 7:12256. https://doi.org/10.1038/s41598-017-12520-2

Ray S, Das SS, Mishra P, Al Khatib AMG (2021) Time Series SARIMA Modelling and Forecasting of Monthly Rainfall and Temperature in the South Asian Countries. Earth Syst Environ 5:531–546. https://doi.org/10.1007/s41748-021-00205-w

Russo S, Dosio A, Graversen RG, et al (2014a) Magnitude of extreme heat waves in present climate and their projection in a warming world. J Geophys Res Atmospheres 119:12,500-12,512. https://doi.org/10.1002/2014JD022098

Stahl K, Tallaksen LM, Hannaford J, van Lanen H a. J (2012) Filling the white space on maps of European runoff trends: estimates from a multi-model ensemble. Hydrol Earth Syst Sci 16:2035–2047. https://doi.org/10.5194/hess-16-2035-2012